



HAL
open science

The Boundary Layer in the Scale-Relativity Theory of Turbulence

Laurent Nottale, Thierry Lehner

► **To cite this version:**

Laurent Nottale, Thierry Lehner. The Boundary Layer in the Scale-Relativity Theory of Turbulence. 2024. hal-04506133

HAL Id: hal-04506133

<https://hal.science/hal-04506133v1>

Preprint submitted on 19 Mar 2024

HAL is a multi-disciplinary open access archive for the deposit and dissemination of scientific research documents, whether they are published or not. The documents may come from teaching and research institutions in France or abroad, or from public or private research centers.

L'archive ouverte pluridisciplinaire **HAL**, est destinée au dépôt et à la diffusion de documents scientifiques de niveau recherche, publiés ou non, émanant des établissements d'enseignement et de recherche français ou étrangers, des laboratoires publics ou privés.

The Boundary Layer in the Scale-Relativity Theory of Turbulence

Laurent Nottale¹ and Thierry Lehner²

Laboratoire Univers et Théories, Observatoire de Paris

Université PSL, Université Paris Cité, CNRS

F-92195 Meudon Cedex, France

¹ laurent.nottale@obspm.fr, ² thierry.lehner@obspm.fr

March 12, 2024

Abstract

We apply the scale-relativity theory of turbulence to the turbulent boundary layer problem. On the basis of Kolmogorov's scaling, the time derivative of the Navier-Stokes equations can be integrated under the form of a macroscopic Schrödinger equation acting in velocity-space. In this equation, the potential coming from pressure gradients takes the form of a quantum harmonic oscillator (QHO) in an universal way. From the properties of QHOs we can then derive the possible values of the ratio of turbulent intensities in the shear flow $R = \sigma_u/\sigma_v = 1.35 \pm 0.05$. We show that the Karman constant is theoretically predicted to be $\kappa = 1/R^3$, in good agreement with its typical value $\kappa \approx 0.4$ and its observed possible variations. Then we find a generic solution of our equations for the normal Reynolds stress pure profile, which closely fits the data from laboratory and numerical experiments. Its amplitude μ_B is solution of an implicit equation that we solve numerically and analytically through power series, yielding to lowest order $\mu_B - 1.35 \approx -2(R - 1.35)$, plus smaller contributions from other parameters. Consequently the correlation coefficient of velocities is given by $\rho \approx 1/R \mu_B^2 \approx 1/R^3 \approx 0.4$ and is therefore equal to the Karman constant to lowest order, in agreement with its universally measured value ≈ 0.4 for all shear flows. We also find a general similarity between turbulent round jets and boundary layers in their outer region. These results therefore apply to a wide set of turbulent flows, including jets, plane boundary layers, and to some extent channels and pipes.

1 Introduction

In the study of turbulence, the plane boundary layer plays a prominent role since the solution of the mean flow based on the asymptotic matching of the inner and outer layers

yields the very important result of the ‘log-law of the wall’ [1, 2]. With the Kolmogorov scaling [K41] [3], this logarithmic velocity profile in the inertial sublayer is indeed one of the major landmarks in turbulence theory. With analytical tools of a rather general nature a very specific result has been obtained, even though the equations of motion cannot be solved in general [4, 5]. This approach became ‘classical’ and was universally applied to all wall-bounded flows. The same logarithmic law and its parameters, in particular the Karman constant $\kappa \approx 0.4$ on which it depends, were considered valid for boundary layers, channels and pipes. Laboratory and numerical experiments suggest that the Karman constant is universal, although with small possible variations of the order of $\sim 5\%$ [6, 7] which has led to question its strict universality [8].

Since, the log-law profile equation and its intrinsic Karman constant are widely used in fluid mechanics. But despite numerous theoretical and empirical attempts to establish formal bases for these concepts, no consensus has been reached [9]. The log law has been theoretically justified through many different arguments and has been advocated for a wide range of wall bounded shear flows (see references in [6, 9]). The value of the Karman constant has been measured through numerous experiments and Direct Numerical Simulations of Navier-Stokes equations [DNS] [6]. Many attempts of theoretical derivations have been made (see review in [9]), but always from merely postulated models instead of the fluid mechanics equations. As a result these theoretical derivations do not concur and the origin of its value remains elusive.

This difficulty can be traced back to a more fundamental and universal problem encountered up to now by all theories of turbulence, namely, the closure problem. When a fluid becomes turbulent, its properties become described not only by the mean velocities but also by their fluctuations described by the Reynolds stresses. As a consequence, the number of equations is smaller than the number of unknowns and the present theory remains incomplete.

In a recent work [10], we have suggested a solution to this closure problem and applied it to turbulent jets by using the scale-relativity approach to turbulence [16, 17, 18]. This has allowed us to obtain theoretical understanding and predictions for the Reynolds stress profiles and for several universal dimensionless quantities such as the jet opening angle $\alpha_J \approx 0.2$, the ratio $R \approx 1.35$ of turbulent intensity amplitudes along the radial direction over the axial one, the mean ratio $X \approx 1/4$ of turbulent intensities over the mean velocity on the jet centerline, and the correlation coefficient of velocities which we have found to be given by $\rho = 1/R^3 \approx 0.4$ [10].

In the present paper we apply the same approach to the turbulent plane boundary layer problem (far from the wall, i.e. in the zone where viscosity becomes negligible), so that it will be relevant to fully developed channel flow, fully developed pipe flow and the flow in a flat-plate boundary layer. These simple flows are of practical importance and played a prominent role in the historical development of the study of turbulent flows [5]. Their description is part of the basic textbook knowledge about turbulence [4, 5, 19, 20], and yet many features characterizing them remain empirical, in particular purely numerical constants such as the Karman constant.

Tennekes and Lumley [4] remark that boundary layer flows are more complicated than

flows in free shear layers (such as in our previous study of the free round jet) because the presence of a solid wall imposes constraints that are absent in wakes and jets. Shear flows are very important to understand turbulence, which is often described as just an instability generated by shear.

The dimensionless character of seemingly universal physical constants appearing in turbulence, such as the Karman constant for boundary layers, makes the understanding of their value one of the most fascinating problems in physics. Moreover, this question is clearly related to a more general problem in the theory of turbulence, namely, the closure problem: when jumping to a turbulent behavior, a fluid is described not only by its mean velocities which are solutions of the continuity and Navier-Stokes equations, but also by the velocity fluctuations. In today's theory there are no known first principle equations for the covariances of these fluctuations (Reynolds stress), which yet appear in the Reynolds-averaged Navier-Stokes (RANS) equations, so that the number of unknowns is larger than the number of equations. The closure is therefore obtained using hypothetical models.

The scale-relativity approach to turbulence [16, 17, 18, 10, 21] is of a different nature. In its framework, the closing equations do not come from an assumed model. They just derive from a reformulation and an integration of the time derivative of the Navier-Stokes equations themselves, written in v -space and accounting for the non-differentiable and fractal nature of velocities in the turbulent regime at inertial scales (according to Kolmogorov K41 scaling). The main result of this approach is that these v -space NS-derived equations can be re-integrated under the form of a macroscopic Schrödinger equation [22, 23, 18]. In this equation, the microscopic Planck constant \hbar is replaced by a new macroscopic constant \hbar_v resulting from the self-organization of the turbulent medium, that is proportional to the rate of dissipated energy ε . The square of the modulus of the wave function which is solution of this equation, $P = |\psi|^2$, yields the probability density distribution (PDF) of turbulent velocity fluctuations, from which the Reynolds stresses can be calculated, thus solving the closure problem.

Moreover, the potential entering this v -Schrödinger equation is, in an universal way, that of an harmonic oscillator [21, 10], so that we can theoretically predict that the local velocity PDF are that of quantized harmonic oscillators (QHO), possibly damped (QDHO). This theoretical expectation has been well verified by an analysis of experimental data [18].

In this paper, we first recall in Sec. 2 the governing equations for the shear flow, which include in our approach both the Reynolds averaged Navier-Stokes (RANS) equations in the boundary layer approximation and the v -space macroscopic Schrödinger equation derived from the Navier-Stokes equations in the turbulent regime. In Sec. 3 we recall some well-known basic theoretical results concerning the turbulent boundary layer, such as the log-law of the wall involving the Karman constant and the derivation of the Reynolds shear stress profile from the RANS equations. In Sec. 4 we recall our theoretical prediction for the possible values of the turbulent intensity ratio $R = \sigma_u/\sigma_v = 1.35 \pm 0.03$ far from the wall, which is similar to its derivation for the round jet [10] from the general properties of QHOs. Then we give in Sec. 5 a general physics argument leading to the conclusion that the Karman constant is given by $\kappa = R^{-3}$, which agrees with its values measured

in laboratory and numerical experiments. The pure (normalized) profile of the normal Reynolds stress σ_v^2 is derived in Sec. 6 from the normal component of the v -Schrödinger equation in a QHO potential. In Sec. 7, an implicit equation is found for its amplitude μ_B^2 from the uv component of the v -Schrödinger equation. We solve this equation both numerically and analytically through power series, thus obtaining an expression of μ_B in function of R , with smaller dependence on other parameters. Then we show in Sec. 8 that, applying relevant scaling factors, the turbulent round jet and the turbulent boundary layer become similar in the region $z \gtrsim 0.2$, where $z = y/\delta$ in the boundary layer and $z = r/\alpha x$ in the jet, being described by the same equations. In Sec. 9, we finally suggest a solution for the puzzle of the value of the coefficient of correlation of velocities, which is found in observations, experiments and direct numerical simulations to be universally equal to $\rho \approx 0.4$ for all shear flows. These results are discussed in Sec. 10 while Sec. 11 is dedicated to the conclusion.

2 Governing equations for the turbulent boundary layer

2.1 RANS equations

We shall study in the present paper the turbulent boundary layer that appears upon a flat plate subjected to a plane flow parallel to the wall. Such a flow is a particular case of a more general ensemble including channels and pipes.

We consider here only the two Cartesian coordinates x along the wall in the direction of the incident flow and y normal to the wall. We use the Reynolds decomposition of velocities $U_t = U + u$, $V_t = V + v$, where $U(x, y)$ and $V(x, y)$ are their average values and u , v their turbulent fluctuations. The fluid mechanics equations for the boundary layer consist of the continuity equation for the mean velocities,

$$\partial_x U + \partial_y V = 0, \quad (1)$$

and of the Reynolds averaged Navier-Stokes (RANS) equations:

$$x\text{RANS} : \quad U \partial_x U + V \partial_y U + \partial_x(\bar{p} + \sigma_u^2) + \partial_y \sigma_{uv} - \nu \Delta U = 0, \quad (2)$$

$$y\text{RANS} : \quad U \partial_x V + V \partial_y V + \partial_y(\bar{p} + \sigma_v^2) + \partial_x \sigma_{uv} - \nu \Delta V = 0, \quad (3)$$

where \bar{p} is the average pressure, $\sigma_u^2 = \langle u^2 \rangle$, $\sigma_v^2 = \langle v^2 \rangle$ and $\sigma_{uv} = \langle uv \rangle$ the Reynolds stresses and where we have taken $\varrho = 1$ for simplification owing to the assumed incompressibility of the fluid.

In the so-called ‘boundary layer approximation’, the terms $\nu \partial_x \partial_x U$, $U \partial_x V$, $V \partial_y V$ and $\nu \Delta V$ are neglected. Moreover, in the turbulent case one may neglect the axial derivative of the Reynolds stresses on the grounds that they are small compared with the lateral gradients [5]. One obtains:

$$U \partial_x U + V \partial_y U = \nu \partial^2 U / \partial y^2 - \partial_y \sigma_{uv} - \partial_x(p_0 + \sigma_u^2 - \sigma_v^2) = 0, \quad (4)$$

$$\bar{p} = p_0(x) - \sigma_v^2. \quad (5)$$

These equations apply to all plane two-dimensional shear flows bounded by quiescent fluid or a uniform stream, such as plane jets, plane mixing layers, plane wakes and boundary layers [5]. Only the boundary conditions differs between these flows, which are all characterized by a characteristic flow width $\delta = \delta(x)$. Except near walls, the viscous term is negligible.

As usual in turbulence, this system of equations is not closed since there are three equations for six unknown, U , V , \bar{p} , σ_{uv} , σ_u and σ_v . The scale-relativity approach to turbulence [16, 17, 18, 21, 10] allows to solve this closure problem by deriving a new expression of the Navier-Stokes equations under turbulent conditions.

2.2 Schrödinger equation in velocity space

The fundamental equation of dynamics can be integrated in the scale-relativity paradigm under the form of a Schrödinger equation, in which the constant is no longer the microscopic Planck constant \hbar but a new macroscopic constant which emerges from self-organization of the system under consideration. Apart from this change of constant, the theory shares the same mathematical structure as standard quantum mechanics, in particular the existence of a wave function which is solution of the Schrödinger equation and whose modulus squared yields the probability density of states.

The conditions which underlie such a transformation are non-differentiability and fractality, which involve an explicit scale dependence of the various variables. We have shown [18] that these conditions (infinite number of virtual trajectories, fractal dimension 2 of each trajectory and two-valuedness of the derivatives as consequence of non-differentiability) are satisfied in velocity space for a turbulent fluid, the fractal dimension 2 being a manifestation of the K41 scaling $\delta v^2 \sim \delta t$.

This method has been recently applied to the turbulent round jet [10] and has allowed us to solve the closure problem in this case. The question raised in the present paper is whether we can obtain a similar result in other type of shear flows, such as flat plate boundary layers, channels and pipes.

Let us summarize our method (see [18, 10] for more details). The time derivative of the NS equations writes in Newtonian form $da/dt = -\nabla \dot{p}$. In order to account for the various geometric effects of non-differentiability and fractality, one replaces d/dt by a new total derivative operator:

$$\frac{\hat{d}}{dt} = \frac{\partial}{\partial t} + \mathcal{A} \cdot \nabla_v - i \mathcal{D}_v \Delta_v. \quad (6)$$

where the acceleration \mathcal{A} is now complex as a manifestation of a fundamental two-valuedness of derivatives implied by non-differentiability. One obtains a new form of the equation of dynamics in v -space:

$$\frac{\hat{d}}{dt} \mathcal{A} = \left(\frac{\partial}{\partial t} + \mathcal{A} \cdot \nabla_v - i \mathcal{D}_v \Delta_v \right) \mathcal{A} = \dot{F}, \quad (7)$$

where F contains the pressure gradient term and possibly any applied external force. Introducing a wave function $\psi_v = e^{i\mathcal{S}_v/\hbar_v}$, where \mathcal{S} is the complex action and \hbar_v the new Planck-like constant in v -space, which is proportional to the rate ε of transferred energy dissipated at viscous scales. One can prove [22, 24, 23, 18] that this equation can be integrated under the form of a macroscopic Schrödinger equation in v -space:

$$\mathcal{D}_v^2 \Delta \psi_v + i \mathcal{D}_v \frac{\partial}{\partial t} \psi_v - \frac{1}{2} \phi_v \psi_v = 0, \quad (8)$$

(with $\mathcal{D}_v = \hbar_v/2$), which yields the PDF of velocities as $P_v = |\psi_v|^2$. In this Schrödinger equation, the potential energy takes the universal form of an harmonic oscillator v -potential [21, 10] which writes when the mean pressure is time-independent:

$$\phi_v(u, v) = \frac{1}{2} \left(\frac{\partial^2 \bar{p}}{\partial x^2} u^2 + 2 \frac{\partial^2 \bar{p}}{\partial x \partial y} u v + \frac{\partial^2 \bar{p}}{\partial y^2} v^2 \right), \quad (9)$$

3 Theoretical elements

We shall recall in this section some well-known basic theoretical results concerning the turbulent boundary layer which will be necessary for our theoretical prediction of the Reynolds stress profiles and of the coefficient of correlation of velocities.

3.1 Thickness of the turbulent boundary layer

It has been shown by Landau [19] that, $c(x)$ being the solution of the equation

$$c \ln(c R_x)^2 = 2\kappa^2, \quad (10)$$

the thickness of the flat plate turbulent boundary layer [FPTBL] is given by:

$$\delta(x) = a_0 x \sqrt{c(x)}. \quad (11)$$

The parameter a_0 is an empirical numerical constant which is not theoretically predicted up to now, for which Landau gives the approximate value $a_0 \approx 0.3$. In this expression $R_x = U x/\nu$ is the x Reynolds number. For $\kappa = 0.4$, one finds that a very good approximation for the solution of this equation is:

$$c(x) = 0.191 R_x^{-2/7}. \quad (12)$$

This leads to a FPTBL thickness:

$$\delta(x) = \delta_0 x R_x^{-1/7}, \quad (13)$$

where $\delta_0 = \sqrt{0.191} a_0 = 0.437 a_0$. This result demonstrates theoretically the $R_x^{-1/7}$ behavior of the BL thickness, with an exponent slightly different from the original Prandtl

value $-1/5$ [25, p. 638]. The numerical constant in this relation is $\delta_0 = 0.16$, which would yield $a_0 = 0.37$, of the order of magnitude of the Landau value.

The wall-friction velocity $v_\star = \sqrt{\sigma/\varrho}$ is given by $v_\star = U\sqrt{c/2}$ [19], i.e.:

$$v_\star = 0.309 U R_x^{-1/7}, \quad (14)$$

where σ is the frictional force acting on the unit area of the wall and ϱ is the fluid density. Actually the effect of the $x^{-1/7}$ variation is negligible, and we shall take in what follows $\delta(x) = \alpha_B x$, with $\alpha_B = 0.16 R_x^{-1/7} = (0.06, 0.05, 0.04, 0.03, 0.02)$ for $R_x = (1000, 3000, 15000, 100000, 2 \times 10^6)$. This can be compared to the turbulent jet, whose half-width is αx , with $\alpha \approx 0.2$.

3.2 Log-law of the wall and Karman constant

The turbulent boundary layer is known to be a two-scale process. This is usually described by using two different normalisations for the distance y along the direction normal to the wall. Far from the wall the flow does no longer depend on the viscosity, so that y is referred to the boundary layer thickness $\delta(x)$, using the dimensionless variable $\eta = y/\delta$. Near the wall the viscosity matters and one defines $y^+ = y v_\star/\nu$, where ν is the molecular viscosity coefficient. Four regions can then be characterized:

- (1) $y^+ = (0 - 5)$, $\eta \approx (0 - 0.0005)$; viscous sublayer; $U = v_\star y^+$.
- (2) $y^+ = (5 - 30)$, $\eta \approx (0.0005 - 0.003)$; buffer layer.
- (3) $y^+ = (30 - 1000)$, $\eta \approx (0.003 - 0.1)$; log-law layer; $U = v_\star(\kappa^{-1} \ln y^+ + B)$, where $\kappa \approx 0.4$ and $B \approx 5$.
- (4) $y^+ = (1000 - 10000)$, $\eta \approx (0.1 - 1)$; outer layer; Coles' wake function correction.

The limit of the viscous sublayer is $y^+ = 2/\kappa = 5$. The point where the linear law and the log-law match is given by $y^+ = B + 6 \approx 11$, yielding the estimate $y^+ = 30$ for the end of the buffer layer.

The log-law profile has been theoretically derived from physics principals [1, 2, 19]. It is a priori valid up to $\eta \approx 0.1$, but remains an excellent approximation in most cases in an overlap layer up to $\eta \approx 0.3$. The empirical parameter κ is Karman constant, for which we suggest here a theoretical prediction yielding $\kappa = (\sigma_v/\sigma_u)^3 \approx 0.4$, in agreement with its experimentally measured values.

Finally, near the edge of the turbulent region, the log law must be corrected in the case of plane boundary layers. The correction takes the form of Coles' wake law [26], $2(\Pi/\kappa) \sin^2(\frac{\pi y}{\delta})$, with a coefficient Π which vanishes for channels and pipes.

3.3 Reynolds shear stress: theoretical profile

It is well known that the Reynolds shear stress σ_{uv} in the boundary layer is almost constant for small η values and given by $\sigma_{uv} = v_\star^2$ [4]. For larger values of η , a rough approximation of its profile is given by $\sigma_{uv} = v_\star^2(1 - \eta)$. A better solution is obtained by integrating the

RANS and continuity equations in the wall normal direction with the assumption that $V = 0$ at the wall [27]:

$$\sigma_{uv} = v_*^2 + y \partial_x(p_0(x) - \sigma_v^2) - U \int \partial_x U dy + 2 \int U \partial_x U dy. \quad (15)$$

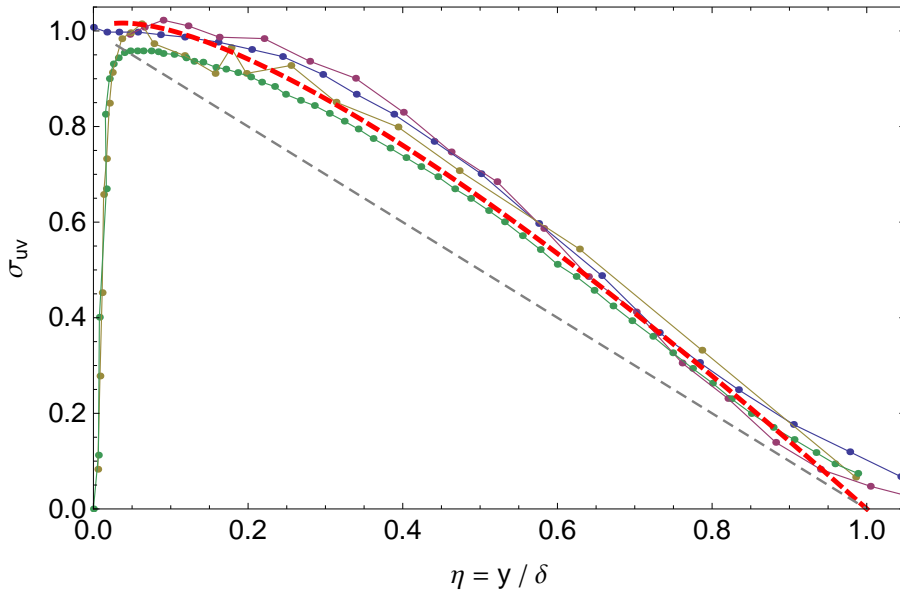


Figure 1: Comparison between the theoretical prediction from RANS and continuity equations of the Reynolds shear stress in the FPTBL (Eq. 17, red dashed curve) and some of its experimental measurements. Green points and curve: Volino and Schultz [27]; Blue: Brennen [12]; Magenta: Erm and Joubert [28]; Brown: Brzek et al. [29]. The gray dashed line is the standard approximative solution $\sigma_{uv} = 1 - \eta$ (normalized to $v_* = 1$).

The term $\partial_x p_0 = -v_*^2/\delta$ yields the standard solution $\sigma_{uv} = v_*^2(1 - \eta)$ [4]. The terms involving the Reynolds stresses are found to be small. The main correction therefore comes from the streamwise velocity U . It is given by the log-law, which remains valid up to $\eta \approx 0.3$ [19]:

$$U = v_* \left(\frac{1}{\kappa} \ln \eta + B \right). \quad (16)$$

One finally finds:

$$\sigma_{uv} = v_*^2 \left[1 - \eta \left(1 + \frac{\alpha_B}{\kappa^2} (\ln \eta + B\kappa - 2) \right) \right]. \quad (17)$$

It is noticeable that, with the empirical numerical values $\kappa = 0.4$ and $B = 5$, the constant $(B\kappa - 2)$ vanishes. The effect of the Coles' correction of the Reynolds shear stress profile in the outer layer is found to be negligible. This theoretical expectation is in good agreement with the experimental measurements, as exemplified in Fig. 1.

4 Theoretical prediction of the ratio of Reynolds stresses

Tennekes and Lumley [4] have argued that the energy in the u component differs from that in the v component because the major production term feeds energy into σ_u^2 (along the axial direction), so that the energy must leak into σ_v^2 (along the radial direction) by inertial interaction. Since the two effects (axial supply and radial leakage) are determined by the same turbulence dynamics, they conclude that $K = (\sigma_u^2 - \sigma_v^2)/(\sigma_u^2 + \sigma_v^2) \approx \text{cst}$ and that it should be less than unity. This implies that $R = \sigma_u/\sigma_v > 1$ should be close to a constant.

We have derived in Ref. [10] the theoretically expected possible values of R by only using a self-evident property of the turbulent jet which appears clearly in this analysis and in the governing equations, namely, the mere fact that $K \geq 0$, i.e. $\sigma_u \geq \sigma_v$. Let us briefly remind here the argument.

We apply this inequality in the scale-relativity framework, where the derivative of the Navier-Stokes equations take a (macroscopic) quantum-like Schrödinger form. We have decomposed the global Gaussian turbulent velocity fluctuations variances σ_u^2 and σ_v^2 in terms of two-dimensional quantized harmonic oscillators (QHOs), which are known to be defined by quantum numbers $\{n_u, n_v\}$.

The above inequality, applied on the various excited states of a 2D QHO, simply becomes $n_u \geq n_v$. As this level of the analysis we take $R = \text{cst}$, in agreement with Tennekes and Lumley's argument.

Our first derivation of the range of possible values for R has been obtained in the framework of the study of the turbulent jet. This has allowed us to consider only the uncorrelated turbulent velocities on the centerline of the jet. This is no longer possible in the BL case where the correlation coefficient may be everywhere different from 0 (and equal to ≈ 0.4 : this is another puzzle for which we suggest a solution hereafter). However, one can show that the velocity correlation has a very small effect on the ratio R in the BL case. Therefore we can write:

$$\sigma_{n_u}^2 = (2n_u + 1) \sigma_{uF}^2, \quad \sigma_{n_v}^2 = (2n_v + 1) \sigma_{vF}^2, \quad (18)$$

where σ_{uF}^2 and σ_{vF}^2 are the variances of the normal (ground) state for the u and v coordinates (the PDFs of which are Gaussian).

In the scale relativity approach, turbulence and its main effects such as intermittency come from the emergence of a new acceleration component which writes $A_q = \pm \mathcal{D}_v(\partial_v P_v)/P_v$ [18]. The probability density P_v of QHO excited states shows zero values $P(v_i) = 0$ for some values of the velocity v_i , which implies the divergence of this acceleration. We have shown that this result explains and accounts in detail for many features of turbulence (large tails of acceleration PDF, structure functions, etc.) [18].

The ground state, for its part, shows no such zeros. We have therefore interpreted its manifestation as corresponding to the transition between laminar and turbulent flow, which occurs around the edge of the turbulent region. This means that, when approaching the edge of the boundary layer, the turbulent fluctuations become that of the ground state, $\sigma_u = \sigma_{uF}$ and $\sigma_v = \sigma_{vF}$. In this regime we expect isotropy of the fluctuations, so that

Figure 2: Expected distribution of values for the ratio $R = \sigma_u/\sigma_v$ when the ground state ratio $R_F = 1$. It is derived from the decomposition of the turbulent fluctuation velocities into QHOs, for a maximum quantum number $n_u = 30$. The density of points increases for higher R values toward ~ 1.41 , but the probability of smaller values toward ~ 1.3 (represented by the point size) is larger according to Gibbs distribution. This yields an average $\langle R \rangle \approx 1.35$.

$\sigma_{uF} \rightarrow \sigma_{vF}$ and therefore $R_F = \sigma_{uF}/\sigma_{vF} \rightarrow 1$ and $R \rightarrow 1$. Experimental data fairly support this expectation, since the turbulent intensities are found to become equal when approaching the boundary layer edge, for $\eta > \approx 0.8$, and R to finally fall down to $R = 1$ at $\eta \approx 0.9 - 1$, as can be seen in Figs. 3 and 16.

The global variances will therefore be $\sigma_u^2 = \langle \sigma_{ui}^2 \rangle$ and $\sigma_v^2 = \langle \sigma_{vi}^2 \rangle$, where the mean is taken on all the QHOs with fluctuating quantum numbers. We find finally:

$$R^2 = \frac{\sigma_u^2}{\sigma_v^2} = \frac{\langle 2n_u + 1 \rangle}{\langle 2n_v + 1 \rangle} R_F^2 \quad (19)$$

for the PDF of n_u given by the Gibbs distribution and $n_v = \{0, 1, 2, \dots, n_u\}$.

When the Reynolds number is large enough, this distribution is almost flat (as a first approximation) and we can take the direct average.

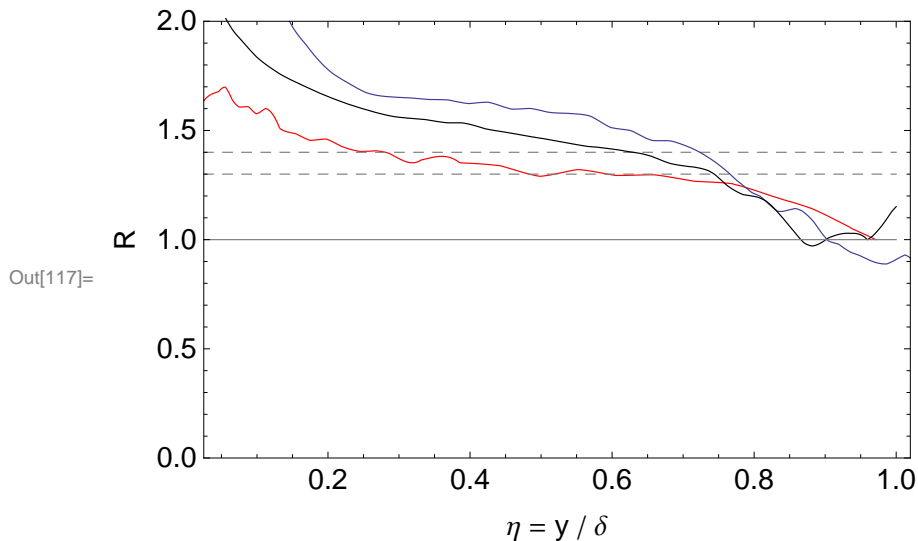


Figure 3: Experimental profiles of the ratio of turbulent intensities $R = \sigma_u/\sigma_v$ across the turbulent region in the direction normal to the plane. The red curve results from Shafi and Antonia data [11], the black curve from Brennen [12] and the blue curve from DNS by Spalart [13, 14]. We have shown as horizontal dashed lines the interval $R = (1.3 - 1.4)$ expected when the ground state ratio $R_F \rightarrow 1$ (approaching the BL edge) and as continuous gray line the value $R = 1$ expected on the edge.

Let us first consider some selected given value of n_u . From statistical physics, one expects only small quantum numbers to play a leading role. For $n_u = 2$, $\langle n_v \rangle = 1$ then when $R_F = 1$ (toward the BL edge), $R = \sqrt{5/3} = 1.29$; for $n_u = 3$, $R = \sqrt{7/4} = 1.32$; for $n_u = 4$, $R = \sqrt{9/5} = 1.34$.

More generally, taking all the values of n_u between 1 and $(n_u)_{max}$, we find the R values given in Fig. 2. Identifying the resulting interval $(1.29 - 1.41)$ with $\pm 2\sigma$, we obtain

$$R_{th} = 1.35 \pm 0.03. \quad (20)$$

This theoretical prediction is in satisfactory agreement with the results of laboratory and numerical experiments in the relevant region (far from the wall), as well for boundary layers as for channels and pipes (see Figs. 3, 4 and 16).

This result is still reinforced by accounting for the expected Gibbs distribution of the QHOs, which favor smaller values of the quantum numbers. The probability for a QHO to be in a given state of quantum number n can be written as [30]:

$$w(n) = e^{-\frac{1}{2}(2n+1)\frac{\hbar_v\omega}{T_v}}, \quad (21)$$

where $T_v = k_B a^2$ is the equivalent of temperature in v -space, $\hbar_v = \varepsilon = \sigma_v^3/L$, $\omega = 2\pi/T$. We have found from Mordant data that $T = NT_L$, with $N \approx 6$, so that $\omega \approx 1/T_L$. We can now relate all these constants to $R_\lambda = \sqrt{15L\sigma_v/\nu}$, since $\sigma_v \sim R_\lambda^2$, $\sigma_a^2 \sim R_\lambda^9$ and

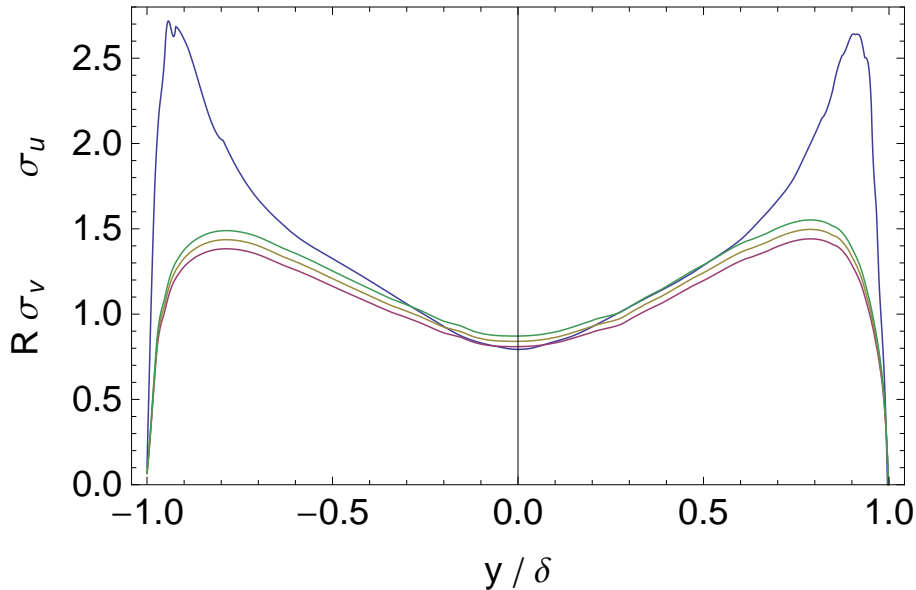


Figure 4: Comparison between the streamwise turbulent intensity profile $\sigma_u(\eta)$ in a channel (blue curve) and the scaled normal turbulent intensity $R \sigma_v(\eta)$, for three values of $R = (1.30, 1.35, 1.40)$ (magenta, brown and green curves), from the DNS data of Kim et al [15]. This supports our theoretical expectation according to which $\sigma_u \approx 1.35 \sigma_v$ in the central region of the channel, far from the walls (which lie at $\eta = \pm 1$).

$T_L \sim R_\lambda^{-2}$. One finally finds:

$$\frac{\hbar_v \omega}{T_v} = \frac{\sqrt{15} \pi C_0}{k_B A_0 N R_\lambda}, \quad (22)$$

where C_0 and A_0 are the two Kolmogorov constants (having values $\approx 4 - 6$), $C_0 = 2\sigma_v^2/\varepsilon T_L$ and $A_0 = \sigma_a^2 \tau_\eta/\varepsilon$. Finally, we find that the constant in the Gibbs distribution is proportional to $1/R_\lambda$. This means, as could be expected, that higher quantum numbers n contribute more for higher Reynolds numbers. Finally the probability can be written under the form:

$$w(n) = \exp \left[-\frac{R_{\lambda_0}}{R_\lambda} \left(n + \frac{1}{2} \right) \right], \quad (23)$$

where the constant $R_{\lambda_0} \approx 100$ from an analysis of Mordant's data.

With this value we find, for fully developed turbulence with reduced Reynolds number $R_\lambda = 1000$ (i.e., $Re \approx 70000$) and maximum quantum numbers respectively $n_{max} = (10, 20, 30)$, mean values of the R ratio $\langle R \rangle = (1.31, 1.33, 1.335)$. For larger values $n_{max} \leq 50$ the mean value of R stabilizes at $\langle R \rangle = 1.34$.

5 Possible solution to the Karman constant problem

It has been argued by Landau [19] about the flat plate boundary layer that this type of flow is characterized by no constant parameter of length which would allow to determine the scale of the turbulent flow. In consequence, he concludes that the main scale of turbulence is determined by the distance itself, i.e., the only available natural scale in the infinite flat plate problem is the height y . Therefore

$$L_x = y. \quad (24)$$

This theoretical expectation is supported by Tennekes and Lumley analysis of the link between Reynolds stress and vortex stretching [4]. They argue that the existence of a Reynolds stress requires that the velocity fluctuations u and v be correlated. The eddies are continuously losing energy to smaller eddies, so that they need shear to maintain their energy: the most powerful eddies thus are those that can absorb energy from the shear flow more effectively than others. They conclude, in agreement with Townsend [31] and Bakewell and Lumley [32], that the eddies which are most effective in both maintaining the u , v correlation and in extracting energy from the mean flow are vortices whose principal axis is roughly aligned with that of the mean strain rate. These three dimensional vortices with vorticity ω are stretched by the rate of strain S with ω parallel to S along a direction making an angle of $\approx 45^\circ$ with the flat plate (see their Fig. 2.5 p. 41).

Experimental observations of these eddies clearly supports this expected angle of 45° (see e.g. [33, 34], and therefore the evidence for the fact that the fundamental length-scale is $L_x = y$.

In the scale-relativity approach to turbulence, the fundamental constant \hbar_V in velocity-space is identical (or at least proportional) to the K41 rate of transferred energy ε . The unicity of this constant implies the relation:

$$\hbar_V = \frac{\sigma_u^3}{L_x} = \frac{\sigma_v^3}{L_y}, \quad (25)$$

which relates the anisotropy of the velocity turbulent fluctuations with the space anisotropy. Therefore:

$$\frac{L_y}{L_x} = \frac{\sigma_v^3}{\sigma_u^3} = \frac{1}{R^3}. \quad (26)$$

Finally the length-scale along the transverse direction is therefore:

$$L_y = \frac{y}{R^3}. \quad (27)$$

The mean streamwise velocity is solution of the differential equation:

$$\frac{dU}{dy} = \frac{v_\star}{L_y} = \frac{R^3 v_\star}{y}, \quad (28)$$

which is integrated under the form of the well-known log-law of the mean velocity profile:

$$U = \frac{v_\star}{\kappa} \ln \frac{y}{y_0}, \quad (29)$$

in which κ is the Karman constant for which we have therefore obtained a theoretical prediction:

$$\kappa = \frac{1}{R^3}. \quad (30)$$

From the previously theoretically estimated range for $R = \sigma_u/\sigma_v = 1.35 \pm 0.03$ we can now derive the possible values of the Karman constant:

$$\kappa = 0.405 \pm 0.025, \quad (31)$$

in good agreement with its measured values.

Actually, statistical analysis of the available data [6] shows that the differences between the three canonical flows could be much larger than the uncertainty in the extracted overlap parameters. This suggests that the von Karman coefficient may not be strictly universal and exhibits a small dependence on the flow geometry.

The mean value of κ has been found to be 0.37, 0.39 and 0.41 respectively for channels, flat plate boundary layers and pipes [6]. These values correspond to respectively $R = 1.39$, 1.37 and 1.35 for $R_F = 1$, which clearly lie in the range expected from the present v -Schrödinger / QHO approach.

More generally, Nagib and Chauhan [6] find a full range of measured values $\kappa = 0.35 - 0.45$. Smart [9] reports the existence of atmospheric measurements showing κ values as low as 0.35 [35] and as high as 0.46 [36] and of direct numerical simulation of boundary layer turbulence revealing κ values that can range from 0.384 ± 0.004 [37] to 0.452 [38].

The full range of observed κ values, 0.35 – 0.46 thus exactly corresponds to just the full range of possible R values (for $R_F = 1$), between $R_{\max} = \sqrt{2} = 1.414$ yielding $\kappa = 2^{-3/2} = 0.35$ to $R_{\min} = \sqrt{5/3} = 1.29$ yielding $\kappa = (3/5)^{3/2} = 0.46$.

6 Solution for the Reynolds stress profile in the normal direction

Neglecting small terms, the RANS equation for the boundary layer yields the general result [4, 5]:

$$p = p_0(x) - \sigma_v^2. \quad (32)$$

Therefore the pressure in the potential of the v -Schrödinger equation can be replaced by the opposite of the Reynolds normal stress. We denote by R_F the ratio of turbulent intensities in the ground state and by G_v the ratio of the velocity fluctuation variance over that of the ground state:

$$R_F = \frac{\sigma_{uF}}{\sigma_{vF}}, \quad G_v = \frac{\sigma_v^2}{\sigma_{vF}^2}. \quad (33)$$

For QHOs, $\sigma_v^2 = (2n_v + 1)\sigma_{vF}^2$ in a given excited state of probability $P(n_v)$ such that $\sum P(n_v) = 1$, so that $G_v = \sum P(n_v)((2n_v + 1))$, where $P(n_v)$ is given by statistical physics [30].

We call ρ_F the coefficient of correlation of velocities in the ground state and L_v the integral length-scale in the normal direction. Then the k_v equation writes [10]:

$$k_v = -\partial_y \partial_y \sigma_v^2 = H \frac{R_F^2 + \rho_F^2}{R_F^2 (1 - \rho_F^2)^2} \sigma_v^2, \quad (34)$$

where

$$H = \frac{G_v^2}{4L_v^2}. \quad (35)$$

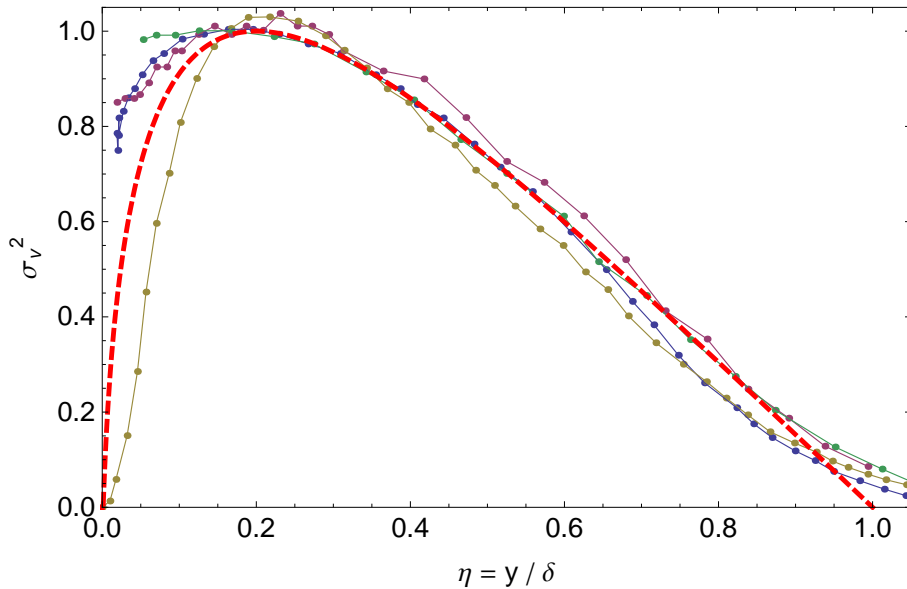


Figure 5: Comparison between our theoretical prediction of the Reynolds stress pure profile σ_v^2/μ_B^2 in a flat plate turbulent boundary layer (red dashed curve, $\eta_P = 0.2$), with some examples of its experimental and DNS measurements. Blue points and curve: Brennen [12]; magenta: Shafi & Antonia [11]; beige: DNS by Spalart [13]; green: Erm and Joubert [28].

One of the main specificities of the turbulent BL with respect to the jet lies in the nature of the integral length scale L_v . As recalled hereabove, it is proportional to the normal distance, $L_v = \kappa y$, the coefficient of proportionality being just the Karman constant which we have theoretically predicted hereabove to be $\kappa = 1/R^3 \approx 0.4$.

Therefore the k_v equation becomes in the FPTBL case:

$$y^2 \partial_y \partial_y \sigma_v^2(y) + B_0 \sigma_v^2(y) = 0, \quad (36)$$

where

$$B_0 = \frac{G_v^2}{4\kappa^2} \frac{(1 + \rho_F^2/R_F^2)}{(1 - \rho_F^2)^2}. \quad (37)$$

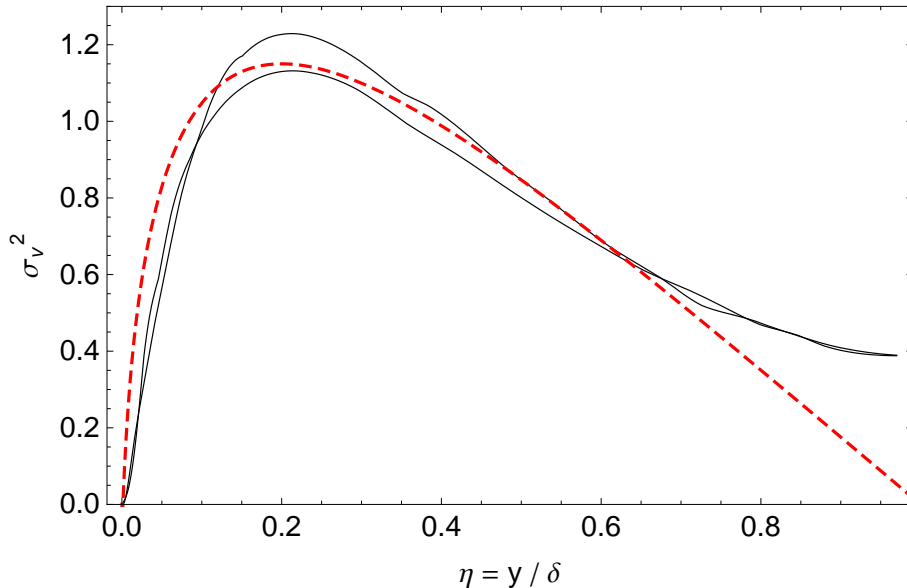


Figure 6: Comparison between our theoretical prediction of the Reynolds stress profile σ_v^2 in a turbulent boundary layer (red dashed curve, $\eta_P = 0.2$), with the result for a channel from DNS by Kim et al. [15]. The two black curves correspond to the up and down parts of the channel. The walls lie at $\eta = 0$ and the centerplane at $\eta = 1$.

This equation is doubly scaling, i.e. invariant under scale factors on both y and σ_v . It can then be equivalently written in terms of the dimensionless normal distance $\eta = y/\delta$. Under the approximation $B_0 \approx \text{cst}$, the solution of this equation writes:

$$\sigma_v^2 = A \sqrt{\eta} \sin(a_P \ln \eta), \quad (38)$$

where $a_P = \sqrt{B_0 - 1/4}$. This function shows interesting multi-scale properties which are reminiscent of the two-scale nature of the flat plate boundary layer [5, 4, 19] (see Appendix A).

It presents a peak at a distance η_P , in terms of which the coefficient a_P writes with a good approximation: $a_P = -0.78313 + 8.108 \eta_P - 9.295 \eta_P^2$, valid for η_P in the range (0.17 – 0.25). An improved expression for a_P is given in Appendix A.

As can be seen in Fig. 5, this theoretical prediction is in good agreement with the results of laboratory and numerical experiments for $\eta_P \approx 0.15 - 0.20$ in turbulent plane boundary layers. In the case of channels and pipes, the edge of the boundary layer $\eta = 1$ for $y = \delta(x)$ is replaced by the center plane of a channel of width $2h$ at $\delta = h$ and the centerline of a pipe of radius r at $\delta = r$. As expected, the behavior of the various functions near $\eta = 1$ becomes different from the free case. We show in Fig. 6 that our theoretical prediction remains nevertheless in good agreement with experiments up to $\eta \approx 0.7$.

Introducing the turbulent intensity amplitude μ_B (unknown at this stage) and the

(known) wall-friction velocity v_* , the full solution writes

$$\sigma_v^2 = \mu_B^2 v_*^2 \sqrt{\frac{\eta}{\eta_P}} \frac{\sin(a_P \ln \eta)}{\sin(a_P \ln \eta_P)}. \quad (39)$$

The situation is therefore comparable to the turbulent round jet case [10] where we have found in the central region of the jet $\sigma_v^2 = \mu^2 U_C^2 \cos(\sqrt{3}\eta/\alpha)$, where $\eta = r/x$ and U_C is the mean axial velocity on the jet centerline. In both cases we have derived from the k_v equation a generic Reynolds stress profile, while the full solution depends also on a numerical amplitude factor (μ_B and μ) and on another numerical factor characterizing the profile shape (η_P and α). These numerical factors can be theoretically derived from other equations, as we shall now see.

7 Theoretical prediction of the turbulent intensity amplitude

We have found hereabove that the k_v equation yields a solution for the pure turbulent intensity profile which agrees with experimental measurements. But, at this level of the analysis, its amplitude remains unknown. As we shall now see, the amplitude μ_B can be obtained from the other equations derived from the QHO v -Schrödinger equation. The method is the same as used for the turbulent jet [10], but now applied to the boundary layer.

7.1 Decorrelation of velocities for QHOs

A direct way to obtain a theoretical solution for the values of μ_B consists of fully solving the equations for the excited states. This can be done by performing a rotation by an angle θ to a coordinate system (\mathcal{U} , \mathcal{V}) where the turbulent velocities become decorrelated. One find this decorrelation angle to be given by:

$$\tan(2\theta) = \frac{2k_{uv}}{k_v - k_u} = \frac{2\sigma_{uv}}{\sigma_u^2 - \sigma_v^2}. \quad (40)$$

Setting $T = \tan(2\theta)$ and $A = 1/\sqrt{1+T^2}$, one obtains:

$$C = \cos \theta = \sqrt{\frac{1+A}{2}}, \quad S = \sin \theta = \sqrt{\frac{1-A}{2}}. \quad (41)$$

The new coefficients $k_{\mathcal{U}}$ and $k_{\mathcal{V}}$ in the QHO potential write:

$$k_{\mathcal{U}} = k_u C^2 - 2k_{uv}CS + k_v S^2, \quad k_{\mathcal{V}} = k_v C^2 + 2k_{uv}CS + k_u S^2. \quad (42)$$

Since $k_{\mathcal{U}\mathcal{V}} = 0$, the two variables are now separated and the expressions of the Reynolds stresses are easily derived from the standard QHO relations:

$$\sigma_{\mathcal{U}}^2 = \frac{(2n_u + 1) \hbar_{\mathcal{V}}}{2\sqrt{k_{\mathcal{U}}}}, \quad \sigma_{\mathcal{V}}^2 = \frac{(2n_v + 1) \hbar_{\mathcal{U}}}{2\sqrt{k_{\mathcal{V}}}}. \quad (43)$$

Finally, we obtain the expressions for the three Reynolds stresses in the initial coordinate system:

$$\sigma_u^2 = C^2 \sigma_{\mathcal{U}}^2 + S^2 \sigma_{\mathcal{V}}^2, \quad \sigma_v^2 = S^2 \sigma_{\mathcal{U}}^2 + C^2 \sigma_{\mathcal{V}}^2, \quad \sigma_{uv} = CS(\sigma_{\mathcal{U}}^2 - \sigma_{\mathcal{V}}^2). \quad (44)$$

7.2 Equation for the amplitude

This system cannot be directly used because of the problem encountered with the k_u equation. In the absence of a source term (up to now unknown), it corresponds to a repulsive harmonic oscillator, which seems to contradict the results of laboratory and numerical experiments.

A solution to this problem consists of using the relation $\sigma_u = R \sigma_v$ and the fact that σ_{uv} is known in order to calculate k_u , instead of using its direct expression $k_u = -\partial_x \partial_x \sigma_v^2$. One obtains:

$$k_u = k_v - k_{uv} \frac{\sigma_v^2}{\sigma_{uv}} (R^2 - 1). \quad (45)$$

Applying this method to the pure normalized profiles (denoted by the subscript o), this yields the following new expressions:

$$k_{uo} = k_{vo} - k_{uvo} (R^2 - 1) \mu^2 \frac{\sigma_{vo}^2}{\sigma_{uvo}}, \quad T = \frac{2\sigma_{uvo}}{\mu^2 (R^2 - 1) \sigma_{vo}^2}, \quad (46)$$

$$k_{\mathcal{U}o} = k_{vo} - k_{uvo} C \left(\frac{\mu^2 (R^2 - 1) \sigma_{vo}^2}{\sigma_{uvo}} C + 2S \right), \quad (47)$$

$$k_{\mathcal{V}o} = k_{vo} - k_{uvo} S \left(\frac{\mu^2 (R^2 - 1) \sigma_{vo}^2}{\sigma_{uvo}} S + 2C \right). \quad (48)$$

As previously seen, the generalized macroscopic Planck constant writes

$$\hbar_V = \frac{\sigma_v^3}{L_{v0}}, \quad (49)$$

where the length-scale must be proportional to y , namely $L_{v0} = \kappa_0 y$. It depends almost linearly on the axial distance since $y = \delta \eta = \alpha_B x \eta$. We have shown in Sec. 3.1 that $\alpha_B = \delta_0 R_x^{-1/7}$, then it depends slightly on x as $x^{-1/7}$. We find that this dependence can be neglected, so that we only describe the Reynolds number dependence considering various values of α_B in the range (0.03 – 0.06) corresponding to $R_x = (10^5 - 10^3)$.

We finally obtain an implicit equation for the turbulent intensity amplitude μ_B ,

$$Q = 2\kappa_0 \alpha_B \eta x \frac{\sigma_{uvo}}{\mu_B^2 \sigma_{vo}^3} \sqrt{1 + \frac{1}{T^2}} \left[\left(n_u + \frac{1}{2} \right) \frac{1}{\sqrt{k_{\mathcal{U}o}}} - \left(n_v + \frac{1}{2} \right) \frac{1}{\sqrt{k_{\mathcal{V}o}}} \right]^{-1} = 1. \quad (50)$$

This equation can be theoretically solved on the basis of our previously acquired knowledge of the pure profile $\sigma_{vo}^2(\eta)$ and of the Reynolds shear stress σ_{uvo} . It therefore depends on the quantum numbers n_u and n_v , on the parameters η_P , R , α_B , and μ_B , and on the scaled radial distance $\eta = r/x$. It is solved by the values of η_P , R , α_B , and μ_B which ensure a

constant radial profile $Q(\eta) = \text{cst}$, provided they exist, and is expected to yield a relation $\mu_B = \mu_B(\eta_P, R, \alpha_B)$. The value of κ_0 can be subsequently derived from the equation $Q = 1$.

As recalled hereabove, statistical physics implies that the states with the smallest quantum numbers are the most probable. However, we have also seen that, in our framework, the ground state $n_u = n_v = 0$ cannot correspond to a fully turbulent state. This is due to the fact that it is devoid of velocity values for which $P_v(v_i) = |\psi_v|^2(v_i) = 0$, while we have identified the zeros of the velocity PDF and the supplementary acceleration component they involve as the source of the main turbulent characteristics [17, 18]. Therefore the ground state is considered to apply only in the turbulent-laminar transition, at the interface between the two regimes.

As a consequence, the most probable state is given by the quantum numbers $n_u = 2$, $n_v = 1$, the other states contributing only in a minor way. We have therefore specifically applied the above equation $Q = \text{cst}$ to this case.

Regarding the Reynolds normal stress pure profile, we have used our theoretical solution normalized to 1 at maximum,

$$\sigma_{vo}^2 = \sqrt{\frac{\eta}{\eta_P}} \frac{\sin(a_P \ln \eta)}{\sin(a_P \ln \eta_P)}, \quad (51)$$

where we recall that $a_P = -0.78313 + 8.108 \eta_P - 9.295 \eta_P^2$.

As concerns the Reynolds shear stress, we have used the solution of the RANS and continuity equations Eq. 17 which writes with a good approximation:

$$\sigma_{uv} = v_*^2 \left(1 - \eta - \frac{\alpha_B}{\kappa^2} \eta \ln \eta \right). \quad (52)$$

We have also considered the usual approximative solution [4] $\sigma_{uvo} = 1 - \eta$ and a polynomial fit of the Reynolds shear stress measurement by Erm and Joubert (EJ, [28]), which writes $\sigma_{uv} = 0.9838 + 0.478\eta - 2.294\eta^2 + 0.872\eta^4$. As we shall see, they yield solutions which frame the more exact solution and are compatible with it.

7.3 Numerical solution by optimization and fit

We have calculated $Q(R, \mu_B, \alpha_B, \eta_P, \kappa)$ for a large range of parameter values, $R = (1.2 - 1.6)$, $\mu_B = (0.8 - 1.6)$, $\alpha_B = (0.03 - 0.06)$, $\eta_P = (0 - 0.4)$ and $\kappa = (0.37 - 0.43)$.

Examples of Q profiles obtained are given in Fig. 7, which demonstrates the existence of very precise solutions for the equation $Q = 1$. The residual standard deviation σ_Q with respect to a flat profile $Q(\eta) = 1$ has been calculated for each set of parameters in the range $\eta = 0.3 - 0.75$. The smallest values of this dispersion reach $\sigma_Q < 0.0002$.

In a run taking $\kappa = 0.4$, a fit of the parameter subset such that $\sigma_Q < 0.002$ yields with a high statistical significance (Student's $t > 80$ for the R coefficients, and > 35 for the others):

$$\mu_B = 9.692 - 10.70R + 3.14R^2 + 1.64\alpha_B + 4.73\eta_P - 18.54\eta_P^2. \quad (53)$$

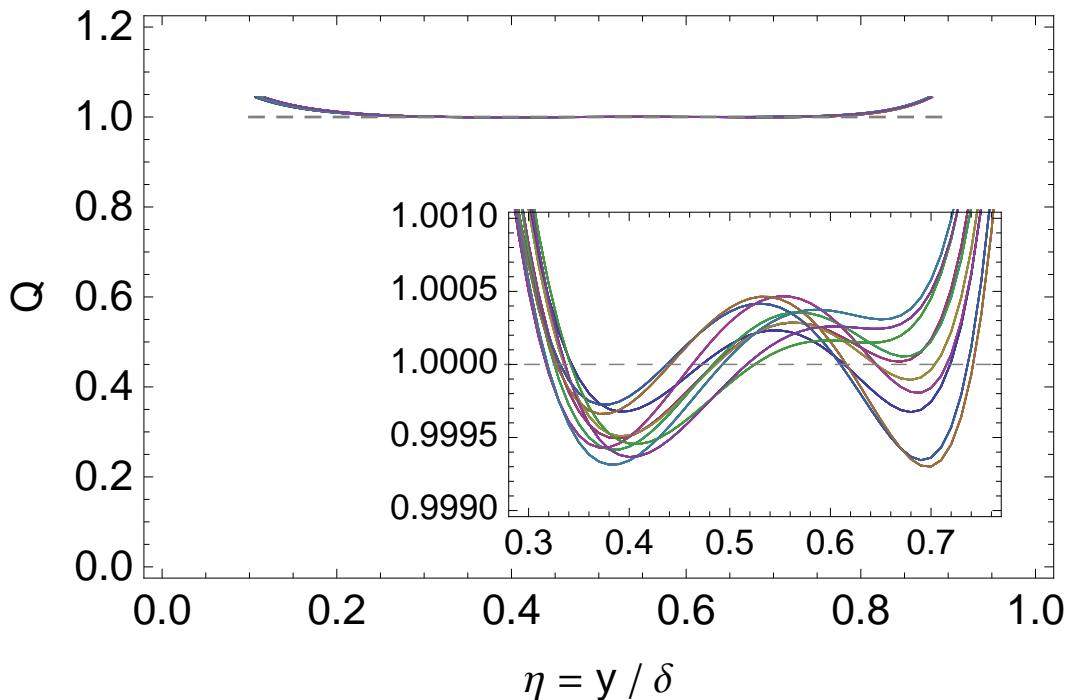


Figure 7: Examples of Q profiles demonstrating that there exists values of the parameters $(R, \alpha_B, \eta_P, \mu_B)$ for which $Q \approx 1$ in a large interval $\eta \approx (0.2 - 0.8)$. The standard deviations for these solutions on the range $(0.3 - 0.75)$ is $\sigma_Q < 0.0003$. The inset is a zoom by a factor ≈ 300 showing the detailed profiles of these solutions.

The dependence of μ_B on α_B and η_P is weak, yielding only small corrections to the mere function of R (see Fig. 22) which can be written under the form:

$$\mu_B(R) = R_0 - 2.26(R - R_0) + 3.11(R - R_0)^2, \quad (54)$$

where $R_0 = 1.344$ is the value for which $\mu_B = R$. This value is just the central value predicted from the QHO Schrödinger equation (Ref. [10] and previous Sec. 4). This result is illustrated in Fig. 8, where we have plotted the values of μ_B in function of R for the various parameters that satisfy $\sigma_Q < 0.002$. In this figure, the values of μ_B have been corrected for the small α_B and η_P dependence according to the above fit Eq. 53.

From the predicted values of $R = 1.34 \pm 0.04$ we therefore derive a theoretical prediction for the range of possible μ_B values, $\mu_B = 1.36 \pm 0.09$, leading to the final conclusion that $\mu_B \approx R \approx 1.35$.

We give in Appendix B the results of our numerical calculations and their fit for different choices of the function $\sigma_{uw}(\eta)$. The agreement between the slopes of the linear term in all cases is remarkable. Only the value for which $\mu_B = R$ changes slightly from 1.33 to 1.35 then 1.38, which remains in the theoretically predicted range of $R = \sigma_u/\sigma_v$.

Finally, the value obtained for the constant κ_0 is compatible with $\kappa_0 = 1$, although with a large dispersion (we find $\kappa_0 = 1.04$ with a standard error $\sigma_{\kappa_0} = 0.30$). This

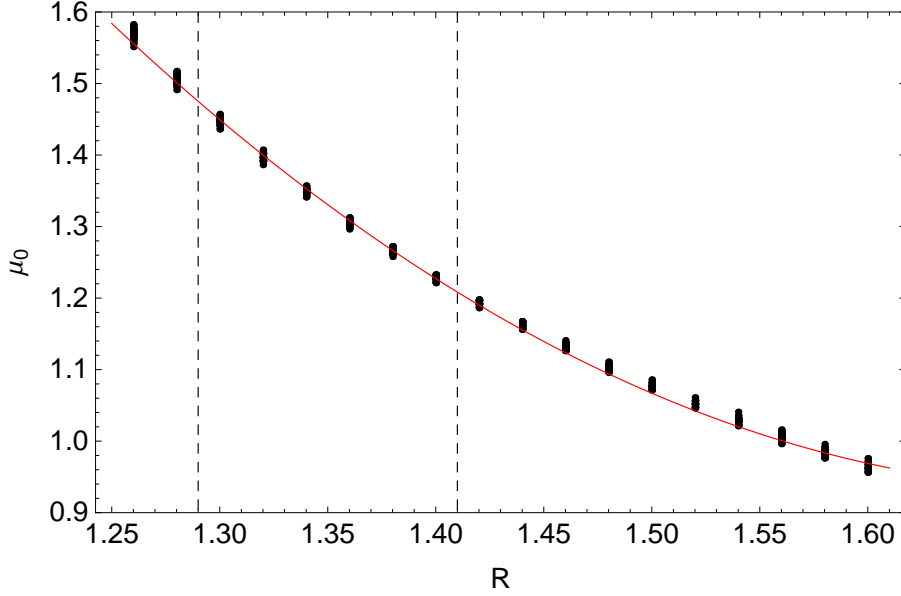


Figure 8: Values of (R, μ_B) solving the equation $Q = \text{cst}$ (Eq. 50), where μ_B is corrected for the small dependence on α_B and η_P . The σ_v profile input in this equation is our theoretical solution of the k_v equation Eq. 38, while the σ_{uv} profile is the solution of the RANS and continuity equations Eq. 52. The red continuous curves is the resulting fit yielding the searched relation $\mu_B = \mu_B(R)$ which is the solution of the equation $Q = 1$. It is indistinguishable in the relevant range $R \approx (1.29 - 1.41)$ from the Series analytic solution given in Eq. 55.

means that the length-scale entering into the definition of the v -Planck constant is just $L_{v0} = \kappa_0 y \approx y$.

7.4 Analytical solution by power series expansion

We have obtained an approximate analytical solution for the function $\mu_B(R, \alpha_B, \eta_P, \kappa)$ by performing a power series expansion of Q in function of η and of the various parameters. We set $n = \eta - \eta_0$, $r = R - R_0$, $m = \mu_B - \mu_{B0}$, $a = \alpha_B - \alpha_{B0}$, $p = \eta_P - \eta_{P0}$ and $k = \kappa - \kappa_0$. The resulting expression of $Q = A + Bn + \mathcal{O}[n^2]$ around $(R_0, \mu_{B0}, \alpha_{B0}, \eta_{P0}, \kappa_0) = (1.35, 1.35, 0.045, 0.16, 0.40)$ to first order in n and to second order in the other parameters is given in Appendix C, Eq. 80.

Then we express the theoretically predicted constancy of Q by requiring the cancellation of the linear term, $B = 0$. This results in the following second order power series expression for $m = \mu_B - 1.35$:

$$\begin{aligned}
m = & (-0.0336 + 1.596a - 0.694p - 0.357k - 13.04ak + 1.29k^2 - 14.90ap + 1.83kp) \\
& + (-2.161 - 5.079a + 1.297p + 0.421k + 62.82ak - 6.75k^2 + 48.91ap - 9.85kp) r \\
& + (4.317 - 39.45a - 2.18p - 6.36k - 177.3ak + 39.7k^2 - 249.5ap + 44.8kp) r^2. \quad (55)
\end{aligned}$$

This function is plotted in Fig. 9 for various values of the parameters. It is in good agreement with the fit of the optimized numerical results, as it can be seen in Figs. 8 and 23.

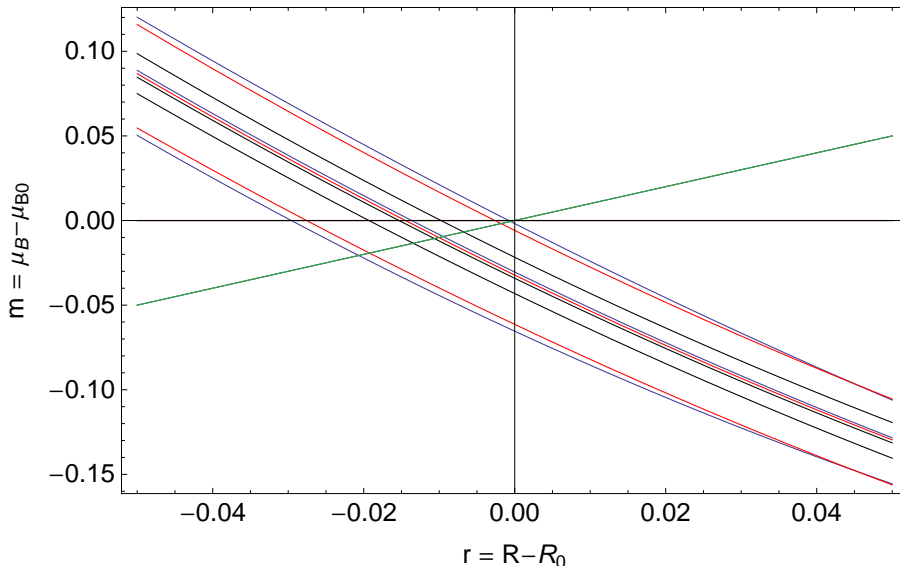


Figure 9: Plot of the analytical function $m(r)$, where $R = R_0 + r$ and $\mu_B = \mu_{B0} + m$ with $R_0 = \mu_{B0} = 1.35$, derived from the equation $Q = \text{cst}$, for various values of the parameters, as given in Eq. 55. The different curves correspond to $a = (-0.02, 0, 0.02)$, i.e. $\alpha_B = (0.025, 0.045, 0.065)$ (blue curves), $p = (-0.04, 0, 0.04)$, i.e. $\eta_P = (0.12, 0.16, 0.20)$ (red curves) and $k = (-0.03, 0, 0.03)$, i.e. $\kappa = (0.37, 0.40, 0.43)$ (black curves). The central values have been slightly displaced for clarity of the plot. The green line shows the values for which $\mu_B = R$.

7.5 PDFs of parameters

The equation $Q = 1$ provides us with a relation $\mu_B = \mu_B(R, \eta_P, \alpha_B, \kappa)$, but also with PDFs for some of the parameters, and therefore with possible theoretical predictions of their values. Indeed, as we shall see, while we have calculated Q for a uniform distribution of the parameters in large intervals, the values of these parameters which yield $Q = \text{cst}$ with a small standard deviation $\sigma_Q \rightarrow 0$ are no longer uniformly distributed. They show either limits not explained by the limits of the initial range, or in some cases well defined and narrow peaks of probability, allowing a theoretical prediction of the most probable values of the parameters and of the standard deviation around these probability peaks.

7.5.1 PDF of α_B

We have performed a specific numerical run for studying the effect of the parameter $\alpha_B = \delta_0 R_x^{-1/7}$ which defines the BL thickness $\delta(x) = \alpha_B x$. We haven taken α_B values

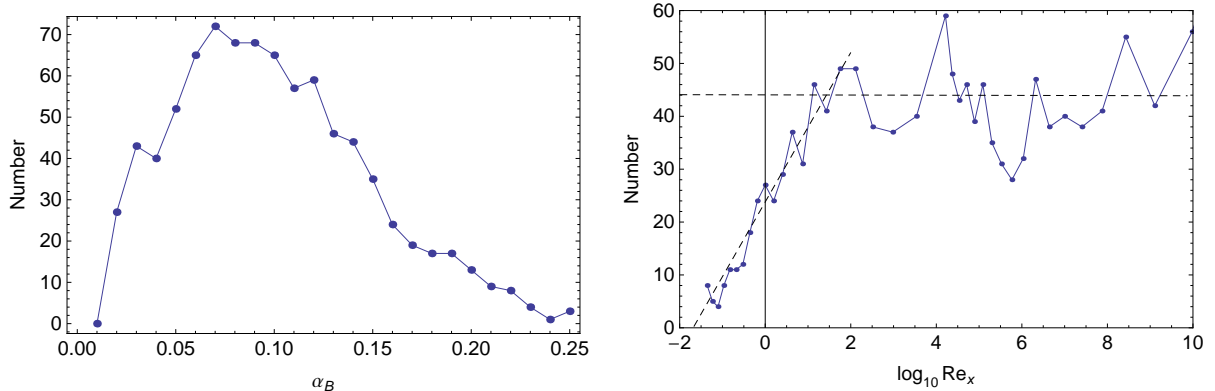


Figure 10: Left figure: PDF of the boundary layer thickness parameter $\alpha_B = 0.16 R_x^{-1/7}$ (with $\delta(x) = \alpha_B x$) obtained from the constraint $Q(\alpha_B, \mu_B, R, \eta_P, \kappa; \eta) = \text{cst}$ by selecting values of the parameters such that the dispersion around $Q = 1$ is $\sigma_Q < 0.003$. Right figure: direct PDF of the Reynolds number R_x under the same conditions, showing a clear transition around $R_x = 1$ for $\delta_0 = 0.16$.

in the range $0.002 - 0.24$ (98290 values of the parameters). The resulting PDF depends of the limit chosen for σ_Q . When $\sigma_Q < 0.01$, one finds a PDF increasing toward small α_B values (large Reynolds numbers) with a peak at $\alpha_B = 0.006$ ($R_x \approx 10^{10}$) and a slower decrease for $\alpha_B > 0.03$ ($R_x < 10^5$). When we take the values of parameters such that $\sigma_Q < 0.003$, one finds a probability peak at $\alpha_B = 0.07$ ($R_x \approx 300$), which is of the order of magnitude of the smallest critical Reynolds number for this kind of flows (see Fig. 10).

Finally one can ask whether a theoretical prediction is possible for the constant δ_0 . We have therefore directly plotted the PDF of R_x for $\delta_0 = 0.16$, as shown in Fig. 10. We find, as could be expected, a flat distribution for large enough Reynolds numbers, but also a very clear transition around $R_x = 1$, which can be interpreted as a theoretical prediction of our chosen value for δ_0 .

7.5.2 PDF of the ratio R of turbulent intensities

The PDF of R is shown in Fig. 11 (left). One finds $1.3 < R < 1.48$ directly from $Q = \text{cst}$ without using neither the value $R = \sqrt{5/3} \approx 1.29$ for $n_u = 2$ and $n_v = 1$, nor the mean result from QHOs, $\langle R \rangle \approx 1.35$. The PDF of μ_B is rather flat since it just reflects that of R and its relation in function of R , $\mu_B \approx 1.35 - 2.25 (R - 1.35)$.

7.5.3 PDF of η_P

In addition, we also find a theoretical prediction for the possible values of η_P , which is such that $\eta_P < 0.24$ with a PDF showing a peak at $\eta_P \approx 0.175$ for $\sigma_Q < 0.007$.

An example of the PDF of η_P is shown in Fig. 11 (right). It shows a well defined peak of probability. However, contrarily to what happens for the other parameters, this peak

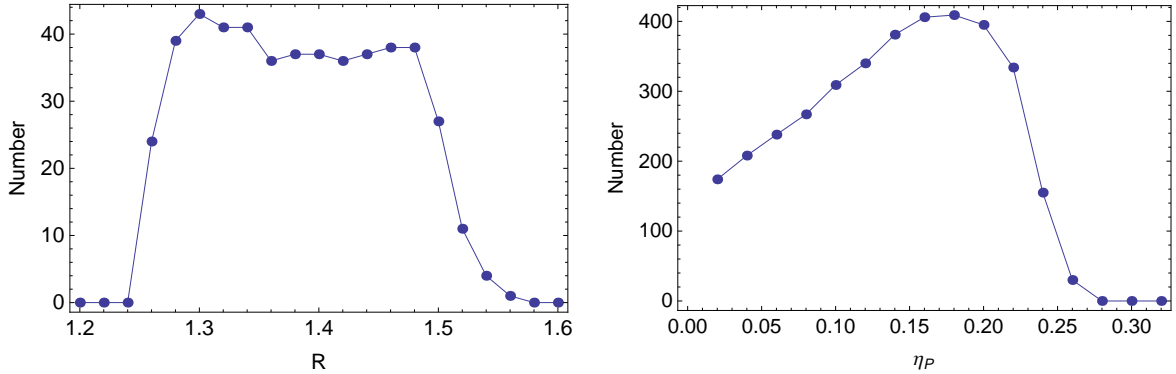


Figure 11: Left figure: PDF of the values of the ratio $R = \sigma_u/\sigma_v$ with satisfy the equation $Q(R, \eta) = 1$ with a standard deviation $\sigma_Q < 0.002$ The initial values were uniformly distributed between 1.2 and 1.6. Right figure: PDF of the values of η_P , which is the position of the maximum of σ_v^2 in our theoretical solution Eq. 51. This PDF is obtained from $\sigma_Q < 0.007$ from initial values of η_P uniformly distributed between 0 and 0.4.

depends on the chosen limit σ_{QL} and varies from $\eta_P = 0.12$ ($\sigma_Q < 0.002$, 490 values) to $\eta_P = 0.2$ ($\sigma_Q < 0.01$, 6432 values). These values agree with the range observed for η_P in boundary layers laboratory and numerical experiments.

7.5.4 PDF and new theoretical prediction of the Karman constant

We show in Fig. 12 an example of the $Q(\eta)$ profiles obtained by varying κ for fixed values of the other parameters. The obtained behavior suggests that a new theoretical prediction for κ is possible from the mere equation $Q = 1$, without resorting to the general argument used in Sec. 5. Actually, the new result obtained here (as we shall see, a probability peak at $\kappa = 0.4$) provides us with a full justification of this argument.

In order to derive a new possible theoretical prediction for the Karman constant κ , we have performed another run with an enlarged interval for the initial values $0.1 < \kappa < 0.5$ (with 116480 differents combinations of the parameters). For this run, the $\mu_B(R)$ function obtained for $\sigma_Q < 0.001$ writes:

$$\mu_B = R_0 - 2.09(R - R_0) + 3.83(R - R_0)^2, \quad (56)$$

with $R_0 = 1.353$. It is in good agreement with the previous determinations of this function.

The resulting PDF of κ is given in Fig. 13. It shows a well marked probability peak at $\kappa = 0.40$ with width ± 0.02 , which is just the range of its experimentally observed values. This is a remarkable result which supports our direct derivation of its value from the turbulent intensity ratio $\kappa = 1/R^3 \approx 0.4$. The effect of the Karman constant in the function $Q(\kappa; \eta) = 1$ comes from its intervention (as $1/\kappa^2$) in the solution of RANS equations Eq. 52 for σ_{uv} . It is itself a manifestation of the mean velocity contribution in the RANS equation, and therefore of the ‘log-law of the wall’ for the streamwise mean

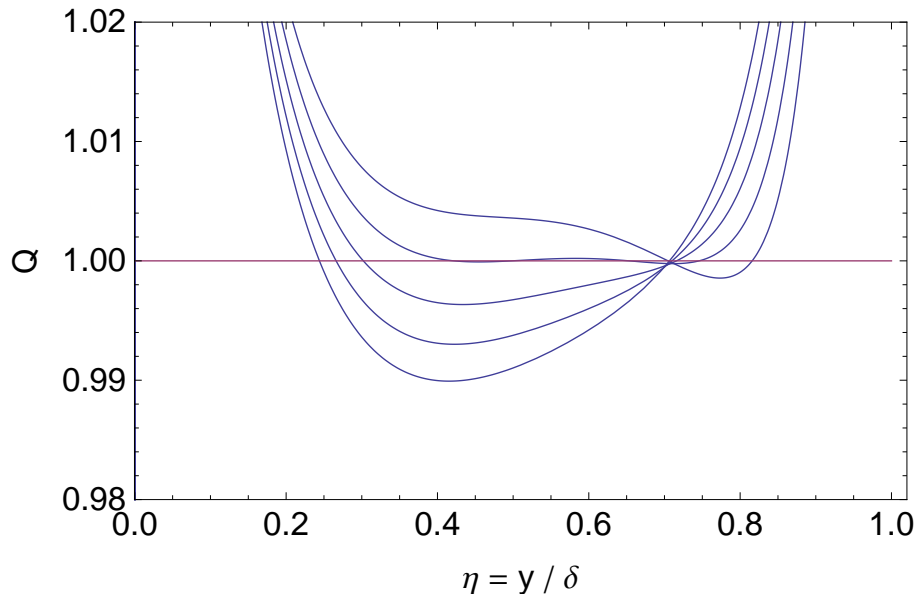


Figure 12: Profiles of the function $Q(\eta)$ along the direction normal to the wall obtained by varying the Karman constant κ for fixed values of the other parameters. The theoretical expectation is a flat profile $Q = 1$. The profiles are plotted for $\kappa = (0.37, 0.38, 0.39, 0.40, 0.41)$ from bottom to top, showing a flat profile for $\kappa = 0.40$ in the range $\eta \approx (0.4 - 0.8)$. The other parameters are in this case $\alpha_B = 0.045$, $\mu_B = R = 1.345$, $\eta_P = 0.15$.

velocity U . In other words, it is the very Karman constant κ of the log-law for which we have found here a theoretical prediction, not only a secondary effect of its value.

This result supports a theoretical numerical value 0.4 ± 0.03 of the Karman constant, but not yet the full and more general relation $\kappa = 1/R^3$. We have therefore constructed the PDF of the variable $g = \kappa R^3$ from the same set of initial values. The result is given in Fig. 14 for $\sigma_Q < 0.001$ and shows a well-defined probability peak around $g = 1$, i.e. $\kappa = 1/R^3$. When the chosen limit σ_{QL} increases, one finds mean values slightly smaller than 1, probably as a result of the bias introduced by keeping values of $Q \neq \text{cst}$. However, the predicted PDF is, strictly, the limit when $\sigma_Q \rightarrow 0$ of the σ_Q dependent PDFs. For $\sigma_Q < 0.0005$, we find $\kappa R^3 = 0.994 \pm 0.039$ (error on the mean) with a dispersion $\sigma_g = 0.146$.

We conclude that the macroscopic QHO v -Schrödinger equation derived in the scale-relativity theory not only predicts the typical value $\kappa = 0.4$ and its possible fluctuations ± 0.03 , but also the full relation $\kappa = 1/R^3$ (that we previously derived from a general physics argument).

7.6 Channels and pipes

Channels and pipes deserve a special treatment, since in their case the equation $Q = 1$ takes a different form. Indeed, the thickness of the turbulent region is no longer dependent on x but must now be considered constant and equal to the half-distance between the

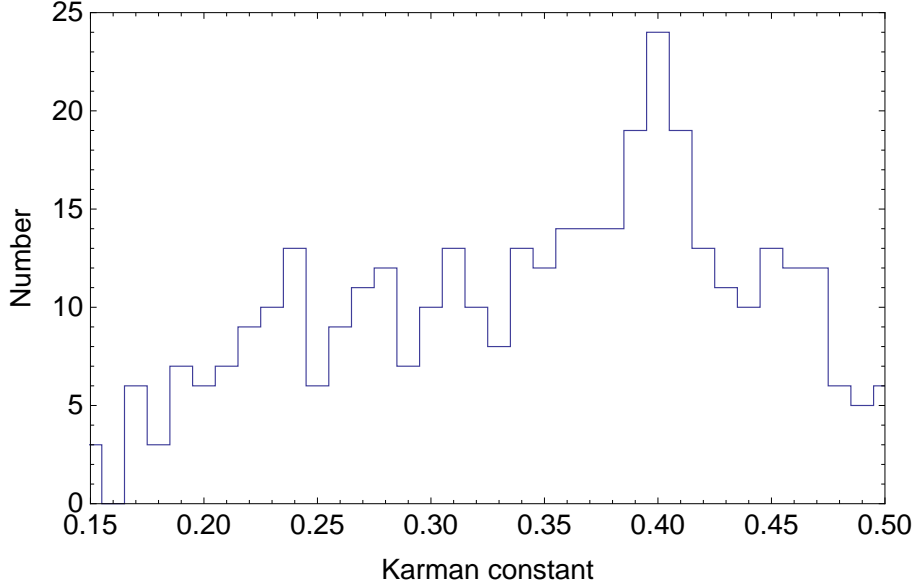


Figure 13: PDF of the values of the Karman constant κ with satisfy the equation $Q(\kappa; \eta) = 1$ with a standard deviation $\sigma_Q < 0.008$. The initial values of κ were uniformly distributed between 0.1 and 0.5.

plates for channels and to the radius for cylindrical pipes. Therefore $\eta = y/\delta$ no longer depends on x , so that the second pressure equation vanishes, $k_{uw} = 0$. In this case one finds a simplified expression:

$$Q_o = 2 \delta \eta \sqrt{k_{vo}} (n_u - n_v) \sqrt{1 + \frac{1}{T^2} \frac{\sigma_{uvo}}{\mu_B^2 \sigma_{vo}^3}}, \quad (57)$$

while $2\delta \eta \sqrt{k_{vo}} = \sqrt{1 + 4a_P^2} \sigma_{vo}$ and $\sigma_{uvo} = \rho R \mu_B^2 \sigma_{vo}^2$. Consequently, setting $\delta n = n_u - n_v$, one finds an explicit solution for μ_B given by:

$$\mu_B^2 = \frac{(1 + 4a_P^2)^{1/2}}{[(Q_o/\delta n)^2 - (a_P^2 + 1/4)(1 - R^2)^2]^{1/2}} \frac{\sigma_{uvo}}{\sigma_{vo}^2}, \quad (58)$$

and for the correlation coefficient of velocities:

$$\rho = \frac{[(Q_o/\delta n)^2 - (a_P^2 + 1/4)(1 - R^2)^2]^{1/2}}{R (1 + 4a_P^2)^{1/2}}. \quad (59)$$

This expression for ρ is independant of the scaled distance $\eta = y/\delta$ to the wall so that we theoretically predict that the velocity correlation coefficient should be constant in the range relevant to our solutions for the Reynolds stresses ($0.2 < \eta < 0/7$).

Another difference for channels and pipes compared with plane boundary layers is the expression for the σ_{uw} profile. Lee and Moser [37] write it under the form $1 - y^+/Re_\tau -$

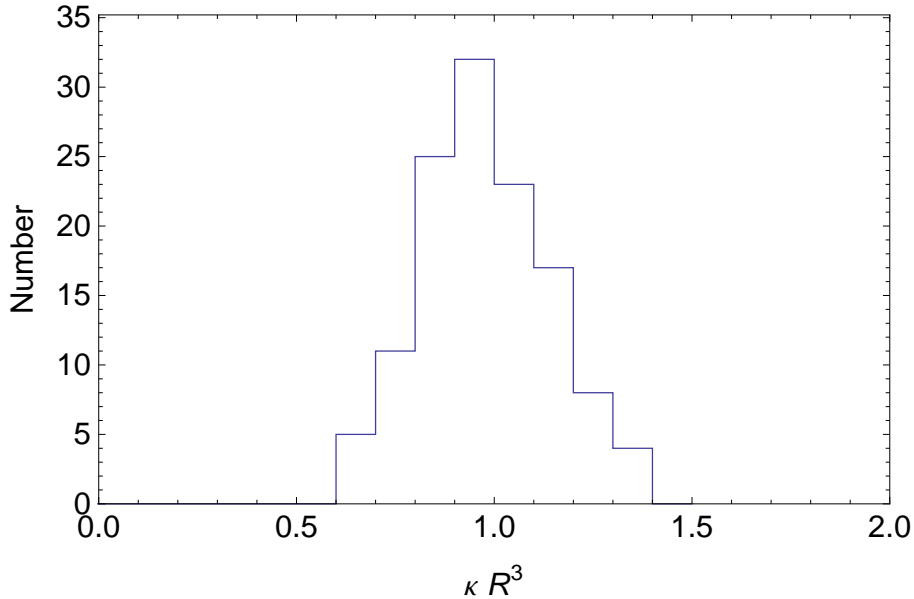


Figure 14: PDF of the variable $g = \kappa R^3$ with satisfy the equation $Q(\kappa; \eta) = 1$ with a standard deviation $\sigma_Q < 0.001$. The initial values of κ were uniformly distributed between 0.1 and 0.5 and those of R between 1.25 and 1.43. The mean value is $g = 0.982 \pm 0.014$ (error on the mean) with a standard deviation $\sigma_g = 0.157$, thus strongly supporting the relation $\kappa = 1/R^3$ to within $\approx 1\sigma$.

$1/\kappa y^+$, which becomes in terms of large scale variables,

$$\sigma_{uvo} = 1 - \eta - \frac{1}{\kappa Re_\tau \eta}. \quad (60)$$

However, we encounter a new problem here, since we expect $Q = \kappa_0 Q_o = 1$ while the exact value of κ_0 , which we have found to be close to 1 for boundary layers, is unknown. Contrarily to the boundary layer case, we cannot use here the constraint $Q = \text{cst}$. Using $\kappa_0 = 1$, we recover the same kind of results as in the BL case, but our theoretical expectation for μ_B becomes less precise in the channel and pipe cases. We intend to perform a specific study of these flows in a forthcoming work [Nottale and Lehner, in preparation].

8 Similarity between the turbulent jet and the turbulent boundary layer

Another way to obtain more directly the amplitude of the Reynolds stress along the direction normal to the wall comes from the existence of a deep analogy between the turbulent jet and the boundary layer. Using this universality we can directly use the result already obtained for the jet [10] and apply it after scaling to the FPBL.

8.1 Universality of Reynolds stress profiles

Let us compare the theoretical solutions for the Reynolds shear stress, derived from the RANS and continuity equations, and for the radial / normal Reynolds stress, derived from the QHO v -Schrödinger equation, in the two cases of turbulent round jet and turbulent flat plate boundary layer (which can be generalized to channels and pipes).

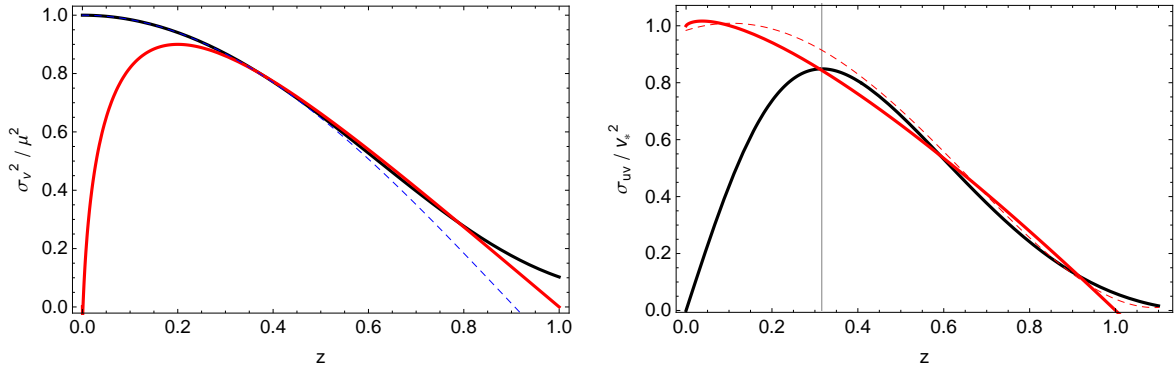


Figure 15: Comparison between the theoretically predicted Reynolds stresses in the free turbulent jet (black curves) and in the flat plate turbulent boundary layer (red curves). The Reynolds shear stresses σ_{uv} are solutions of the continuity and RANS equations, [10] for the jet and Eq. 52 for the boundary layer. The red dashed curve is a polynomial fit of [EJ] data. The Reynolds stresses σ_v^2 are solutions of the QHO v -Schrödinger equation: stretched cosine solution Eq. 61 for the jet and Eq. 51 for the boundary layer. The blue dashed curve is the cosine solution without the stretching term, which is valid in the jet central region. A double scaling is applied in order to manifest the similarity of the solutions (see text).

We have obtained in Ref. [10] precise solutions for the mean velocities U and V and for the Reynolds shear stress $\sigma_{uv} = \eta U^2 - UV$ in the turbulent round jet, by matching inner solutions to the Landau exact laminar outer solution [19]. The radial Reynolds stress has been theoretically derived as solution of the k_v equation:

$$\sigma_{Jv}^2 = \mu^2 U_C^2 \cos\left(\frac{\sqrt{3} z}{1 + a_4 z^4}\right), \quad (61)$$

where U_C is the mean centerline velocity and $z = r/\delta = r/(\alpha x)$ is the normalized radial distance and where the amplitude $\mu = (0.20 \pm 0.015)$ and the coefficient $a_4 = 0.18$ have also been theoretically derived from the QHO v -Schrödinger equation.

In the present paper, we have obtained solutions for the same quantities in the turbulent boundary layer. These solutions are expressed in terms of the wall-friction velocity $v_* = \sqrt{\sigma/\varrho}$ as $\sigma_v^2 = \mu_B^2 v_*^2 \sigma_{vo}^2$ and $\sigma_{uv} = v_*^2 \sigma_{uvo}$. The boundary conditions are very different between the jet and the boundary layer as regards mean velocities, whose variations are reversed, and as regards the central region, since the flow behavior in the BL when

$y \rightarrow 0$ becomes strongly dependent on the viscosity. However both systems come under the boundary layer approximation of the RANS equations and, in the scale-relativity approach to turbulence developed here, are described by the same v -Schrödinger equation.

We therefore expect the two flows to be similar as concerns the turbulent fluctuations in the median and edge regions once proper scaling is applied.

Firstly the distance to be used is naturally the distance ratio to the edge $z = \eta = y/\delta = y/(\alpha_B x)$ for the BL and its equivalent in the jet, $z = r/\delta = r/(\alpha x)$. The analogy is made with the turbulent *round* jet since its scaling in function of the radial distance is $\sim x$ as the turbulent BL while the plane jet would be $\sim \sqrt{x}$, like the laminar BL.

Secondly we expect from our analysis that a velocity $v_{J\star}$ could be defined for the turbulent jet in analogy with the BL velocity v_\star . Such a characteristic velocity should be such that $\sigma_v^2 = \mu_0^2 v_{J\star}^2 \sigma_{vo}^2$ and $\sigma_{uv} = v_{J\star}^2 \sigma_{uvo}$ for the jet.

We show in Fig. 15 a comparison of the theoretically predicted profiles after such a double scaling, for $v_{J\star} = 0.145 U_C$. An excellent agreement is indeed obtained between the σ_v^2 profiles in the range $z \approx (0.2 - 0.9)$, i.e. in about the outer 3/4th of the turbulent region. Since $p = -\sigma_v^2$ in both cases, this means that the potential in the v -Schrödinger equation is the same in this range. This result definitively proves the identity of the turbulent fluctuation equations in the median region of the turbulent domain. Laboratory and numerical experiments fairly support this result, as can be seen in the examples of Fig. 16.

8.2 Consequence: prediction of BL turbulent intensity amplitude from jet amplitude

This remarkable similarity between the jet and the boundary layer turbulent fluctuations allows one to directly derive the amplitude of the BL turbulent intensity μ_B along the direction normal to the plate from the jet radial amplitude μ_J . It reads:

$$\mu_B = \mu_J \frac{\sigma_{vo}^J}{\sigma_{vo}^B} \sqrt{\frac{\sigma_{uv}^B}{\sigma_{uv}^J}}, \quad (62)$$

where the index J stand for the jet and B for the boundary layer.

Using our solutions for the jet [10] and for the boundary layer (present paper), we find a theoretical prediction for the ratio μ_B/μ_J which is shown in Fig. 17 for various values of the parameters. As expected, it is almost constant in function of the variable $z = r/\alpha x$ (round jet) and $z = y/\alpha_B x$ (BL) in the relevant range $z = (0.3 - 0.8)$. Its value, $\mu_B/\mu_J \approx 6 - 7$ yields a theoretical explanation for the observed ratio (0.14 - 0.15) between $v_{J\star}$ and U_C (see Fig. 16).

From the theoretically predicted range $\mu_J = 0.20 \pm 0.015$ [10], one obtains $\mu_B = 1.35 \pm 0.15$, in good agreement with its direct determination.

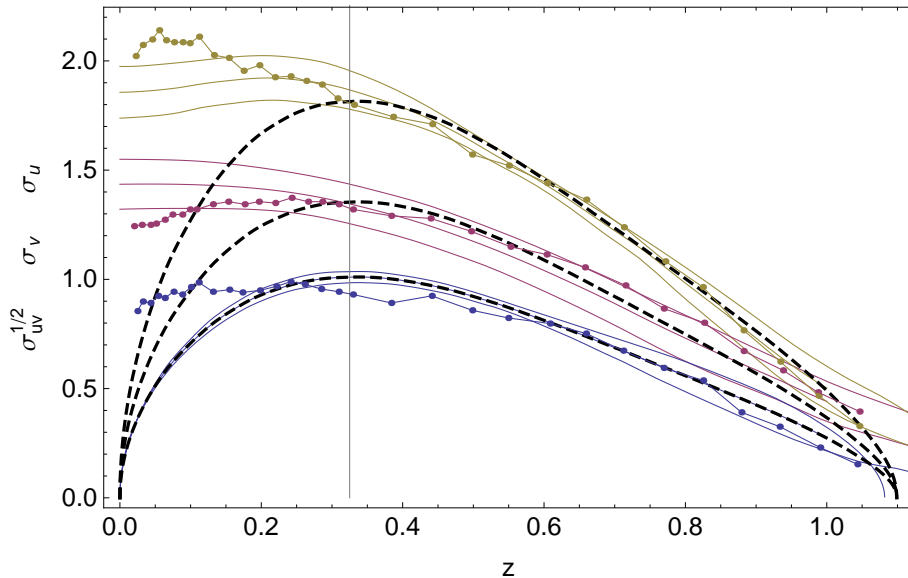


Figure 16: Comparison between the Reynolds stresses in the free turbulent jet and in the flat plate turbulent boundary layer. The blue, magenta and brown continuous lines are measurements of respectively $\sigma_{uv}^{1/2}$, σ_v and σ_u in the free jet by Panchapakesan and Lumley [PL] [39], Hussein et al. [HCG] [40] and their mean. They have been normalized by a velocity $v_{J\star} = 0.14U_C$, where $U_C = U_0 a_0/x$ is the mean centerline velocity, and plotted in function of the scaled variable $z = r/\alpha x$. The irregular blue, magenta and brown lines with points are measurements of the same quantities in a flat plate boundary layer by Shafi and Antonia [11], plotted in function of $z = y/\delta$. The black dashed curves show $v_0(z)/v_{J\star}$, $R v_0(z)/v_{J\star}$ and $R^2 v_0(z)/v_{J\star}$ from $v_0(z) = \sigma_{uv}^{1/2}$ given by the mean of PL and HCG measurements, with $R = \sigma_u/\sigma_v = 1.35$.

9 Theoretical prediction of the velocity correlation coefficient

One of the main mysteries of turbulence is the universality of the correlation coefficient of velocities which is known to be $\rho \approx 0.4$ for all shear flows [4, 5]. We have given a theoretical explanation for this value in the turbulent round jet case, where we have found $\rho = 1/R^3$ [10]. We are now in position to generalize this result to many other flows, such as plane boundary layers, channels and pipes.

The first and shortest way to obtain the result $\rho = 1/R^3 \approx 0.4$ consists of using the similarity found hereabove between the turbulent round jet and the plane boundary layer, which implies that the jet result is also valid for boundary layers. The new information brought here is the identity between the Karman constant and the velocity correlation coefficient, both being given by R^{-3} to lowest order, in agreement with their common experimentally measured numerical value ≈ 0.4 .

There is another direct way toward this result: the general form given to the Reynolds stresses using the characteristic velocity v_\star , which we have shown to be valid both for the

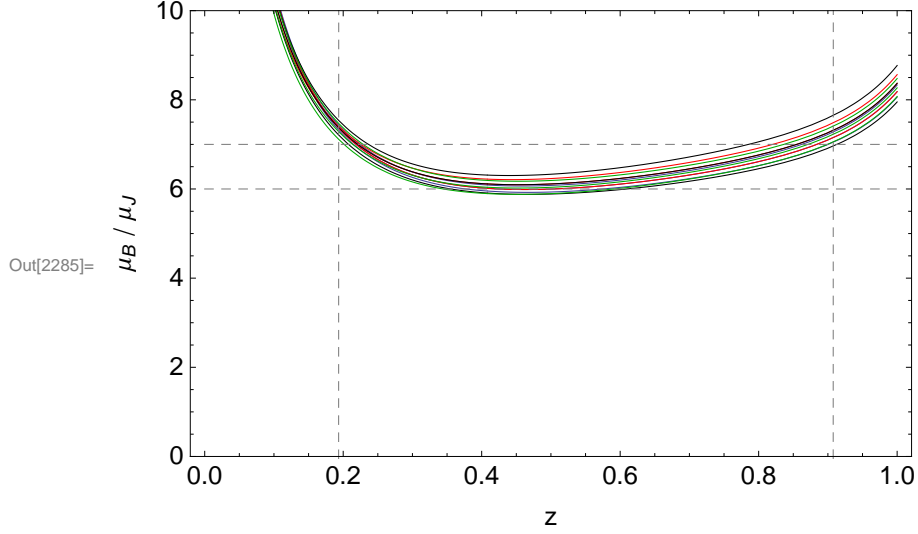


Figure 17: Theoretical expectation of the ratio μ_B/μ_J between the Boundary Layer and the round Jet turbulent intensity amplitudes, as given by Eq. 62. The variable z denotes the normalized distance along the radial direction $z = r/(\alpha x)$ for the round jet and along the direction normal to the wall $z = y/(\alpha_B x)$ for the boundary layer, where x is the axial direction along the streamwise velocity. The different curves correspond to different values of the parameters: $\kappa = (0.37, 0.4, 0.43)$ (blue curves); $\eta_P = (0.15, 0.175, 0.20)$ (red curves); $\alpha_B = (0.025, 0.045, 0.065)$ (black curves); $\alpha = (0.195, 0.205, 0.215)$ (green curves).

turbulent jet and boundary layers (see Fig. 16), allows us to now solve the problem in a fast way.

Indeed, the coefficient of correlation of velocities is given by:

$$\rho = \frac{\sigma_{uv}}{\sigma_u \sigma_v} = \frac{\sigma_{uv}}{R \sigma_v^2} = \frac{1}{R \mu_B^2} \frac{\sigma_{uvo}}{\sigma_{vo}^2}. \quad (63)$$

With the normalized Reynolds stresses $\sigma_{uvo} \sim 1$ and $\sigma_{vo}^2 \sim 1$ around $z \approx 0.2$ (by construction), we get $\rho \approx 1/(R \mu_B^2)$, i.e., to lowest order, knowing that $R \approx \mu_B \approx R_0 = 1.35$,

$$\rho \approx \frac{1}{R_0^3} \approx 0.4, \quad (64)$$

which is the well-known universal experimental value of the correlation coefficient for all shear flows [4]. This value is therefore now theoretically established for round jets, plane boundary layers, channels and pipes ([10] and present paper).

In a more elaborated way, using our explicit expressions for the Reynolds stresses, the coefficient of correlation of velocities writes for the flat plate turbulent boundary layer:

$$\rho = \frac{\sigma_{uv}}{R \sigma_v^2} = \frac{\sqrt{\eta_P} \sin(a_P \ln \eta_P) (1 - \eta - \frac{\alpha_B}{\kappa^2} \eta \ln \eta)}{R \mu_B^2 \sqrt{\eta} \sin(a_P \ln \eta)}. \quad (65)$$

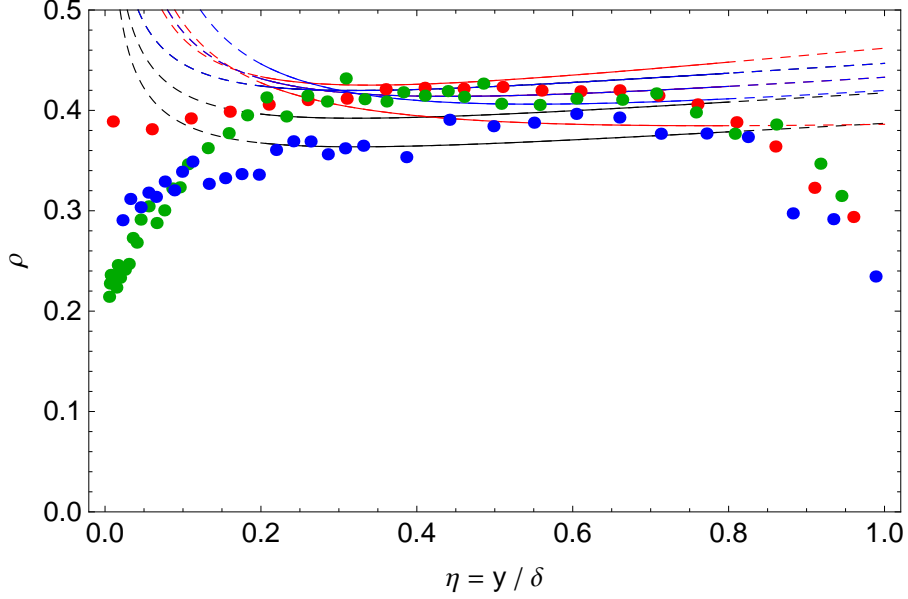


Figure 18: Predicted profile of the correlation coefficient of the (u, v) velocities, for various values of the parameters. We find that it is practically constant on the relevant range $\eta \approx (0.2 - 0.8)$ where the approximation $R = \text{cst}$ holds. The values of the parameters are: $\kappa = 0.4$, $R = (1.34, 1.37, 1.4)$, black curves; $\alpha_B = (0.01, 0.045, 0.07)$, red curves; $\eta_P = (0.12, 0.16, 0.20)$, blue curves. The variation with κ is very weak, as expected from the direct reformulation of the equation $1/Q = \text{cst}$ (Eq. 68), which no longer depend on it. We compare this almost constant theoretical profile to values derived from experimental data: Sillero et al [41], red points; Shafi and Antonia [11], blue points; Gungor et al. [42], green points.

Using the analytical expression we have found for μ_B , we obtain quasi constant profiles $\rho \approx 0.4$ for the coefficient of correlation in the relevant interval $\eta \approx (0.2 - 1)$, as shown in Fig. 18, with variations $< \approx \pm 0.03$ depending on the values of the parameters.

In another way to get this result, the equation $Q = \text{cst}$ can also be directly reformulated in terms of the correlation coefficient ρ . The resulting equation no longer depends on σ_{uv} and therefore on the Karman constant κ . The decorrelation angle θ is given by $T = \tan(2\theta)$, which takes now a new form in terms of R and ρ :

$$T = \frac{2R}{R^2 - 1} \rho, \quad (66)$$

and also

$$k_{Uo} = k_{vo} - k_{uvo} \frac{1}{T} \left(1 + \frac{1 - T^2}{\sqrt{1 + T^2}} \right), \quad k_{Vo} = k_{vo} - k_{uvo} \frac{1}{T} \left(1 - \frac{1 - T^2}{\sqrt{1 + T^2}} \right). \quad (67)$$

We set as before $W_{Uo} = 1/\sqrt{k_{Uo}}$ and $W_{Vo} = 1/\sqrt{k_{Vo}}$. Then we obtain a new form for the equation $S = 1/Q = 1$:

$$S_o = \frac{\sigma_{vo}}{\alpha_B x \eta (R^2 - 1) \sqrt{1 + T^2}} ((n_u + 1/2)W_{Uo} - (n_v + 1/2)W_{Vo}), \quad (68)$$

with $S_o = 2\kappa_0 S$.

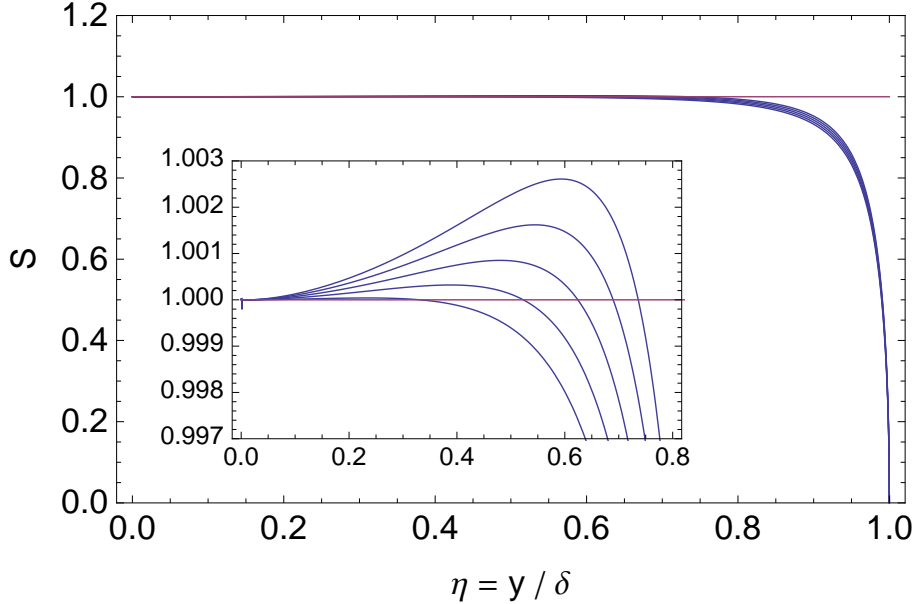


Figure 19: Profile $S(\eta)$ from Eq. 68 obtained for $T = (1.18, 1.185, 1.19, 1.195, 1.20)$, where $T = 2R\rho/(R^2 - 1)$ and $nu = 2$, $nv = 1$, $\eta_P = 0.20$ and $\alpha_B = 0.045$. It remains almost constant as theoretically expected, here on the range $\eta = (0, 0.8)$. The inset is an enlarged view showing that the small differences with $S = 1/Q = 1$ are of order a few 10^{-3} .

We find that $S = \text{cst}$ for a limited range of values of the parameter $T \approx (1.18 - 1.20)$, as can be seen in Fig. 19. From this range we find $\rho = (0.36 - 0.41)$ for $R = (1.35 - 1.40)$, which is compatible with the interval of values obtained from directly inserting the function $\mu_B(r, a, p, k)$ in the ρ expression Eq. 65.

10 Discussion

Despite the obtention of many new results from the scale-relativity theory of turbulence, such as theoretical predictions of the Karman constant value and of its variations, of the normal Reynolds stress profile and of its amplitude, or of the velocity correlation coefficient, there remains some problems and open questions which require further work.

A first problem is that, as in the turbulent jet case, the k_u equation cannot be used in the boundary layer study since it yields a repulsive harmonic oscillator solution for the u velocity fluctuations on most of the normal profile. We have circumvented this problem by setting $\sigma_u = R \sigma_v$ following Tennekes and Lumley argument [4] and using only the k_v and k_{uv} equations. However, this problem seems to point to the fact that the axial component of the velocity-space Schrödinger equation, i.e. along the streamwise flow, is incorrect or incomplete. A more thorough analysis of this problem will be needed.

Another possible drawback concerns the k_v equation, which depends on a parameter B_0 which we have assumed to be constant. Under this hypothesis, this parameter is replaced by the equivalent parameter a_P which can be finally expressed in terms of η_P , the position of the maximum of $\sigma_v(\eta)$. This constancy hypothesis is strongly supported by the excellent agreement obtained between our theoretical profile solution of the k_v equation and the experimental and numerical data. However, both the consistency of the values of B_0 corresponding to its various constituents and its constancy may be questioned and should be studied in more detail.

Using Landau's remark that there is no fixed available scale in the boundary layer problem, so that only y can be used, has led us to suggest that the natural length-scale in the axial direction is $L_x = y$, so that $L_y = R^{-3}L_x$ from the unity of the macroscopic Planck constant, implying a Karman constant $\kappa = R^{-3} \approx 0.4$. One could argue against this reasoning that L_x should be defined up to another unknown numerical constant, i.e. $L_x = k y$. However we have also obtained the same result from the PDF of the variable $g = \kappa R^3$, which shows a well-defined probability peak at $g = 1$. Since this PDF is derived from the constraint $Q = \text{cst}$, i.e., directly from the v -Schrödinger equation (which is itself a re-formulation of the Navier-Stokes equations in the turbulent K41 regime), we consider that this result comes in support of our general physics argument à la Landau.

Further studies are needed to tackle some questions which have not been addressed in the present work, such as that of the lateral Reynolds stress profile $\sigma_w^2(\eta)$, or that of the origin of the possible values of Coles' wake law parameter, which is known only empirically.

Another incompleteness concerns the values of the QHO quantum numbers in the $Q = 1$ equation, which we have taken to be $n_u = 2$ and $n_v = 1$ as representing the most probable excited state. A full solution would involve performing the same analysis for all states and combining them according to their probability densities predicted by statistical physics.

We intend to tackle these open questions in a forthcoming study. We shall also analyse in more detail the theoretically predicted dependence of various quantities like κ and ρ in function of other parameters such as α_B (and therefore the Reynolds number). This dependence, which we have found to be small, may offer an explanation of the experimentally observed behavior of these quantities, which show both a global universality (e.g. $\kappa \approx 0.4$) and small variations possibly depending on flow conditions (e.g. $\kappa = 0.37, 0.39$ and 0.41 respectively for channels, boundary layers and pipes [6]). Our theoretical predictions offer the ability to test for these variations by searching for correlations with the relevant parameters in experimental and numerical data.

11 Conclusion

We have applied in the present work the scale-relativity approach to the plane turbulent boundary layer problem, which concerns also to some extent channel and pipes. We have concentrated our analysis on the outer region far from the wall $\eta = y/\delta > \approx 0.1$ which

allows to neglect the effect of viscosity. Moreover, the intermediate region $0.1 < \eta < 0.3$ has the advantage to be still well described by the ‘law of the wall’ as regards the mean velocity in boundary layers (and even farther for channels and pipes). This allows matching of inner and outer solutions.

In the scale-relativity theory, we have shown that the effect of a non-differentiable and fractal space or medium is to transform the fundamental equation of dynamics into a macroscopic Schrödinger-like equation. Applied to fluid mechanics and in velocity-space [16], this means that the Navier-Stokes equations, once derivated in time and re-integrated in velocity, are transformed in terms of a v -Schrödinger equation in which the potential is a manifestation of the pressure gradient. We have shown that it takes in an universal way the form of an harmonic oscillator potential [10, 21].

Under the boundary layer approximation, which is valid in many flows such as jets, flat plate boundary layers, channels and pipes, the pressure is the opposite of the Reynolds stress, i.e. $p = -\sigma_v^2$. The potential in the v -Schrödinger equation is therefore given by the derivatives of the normal Reynolds stress, which ensures solving the closure problem in these cases.

In this framework, we have been able to theoretically predict quantities which are fundamental to turbulence, such as the Karman constant κ , the ratio of turbulent intensities $R = \sigma_u/\sigma_v$, the profile and amplitude μ_B^2 of the Reynolds stress σ_v^2 along the direction normal to the wall and the coefficient of correlation of velocities ρ . These predictions, according to which $\mu_B = R \approx 1.35$ and $\kappa = \rho = R^{-3} = 0.4$ to lowest order, are in fair agreement with the data from observations and from laboratory and numerical experiments. In particular, the well known puzzle of the universality of the value $\rho \approx 0.4$ of the velocity correlation coefficient in all shear flows [4] has now received a beginning of explanation, being theoretically predicted by the scale-relativity / macroscopic Schrödinger equation approach for round jets [10], plane boundary layers, channels and pipes.

Appendix A: properties of the Reynolds stress solution

We have found a solution to the v -Schrödinger equation for the Reynolds stress σ_v^2 , which writes:

$$\sigma_v^2 = A \mu_B^2 v_*^2 \sqrt{\eta} \sin(a_P \ln \eta). \quad (69)$$

The normalized coordinate is $\eta = y/\delta$, where y is the distance normal to the wall and δ the width of the turbulent zone. Calling η_P the position of the peak of this function, the normalisation factor is given by $A^{-1} = \sqrt{\eta_P} \sin(a_P \ln \eta_P)$, so that the peak value is $\sigma_{vP}^2 = \mu_B^2 v_*^2$, which defines the amplitude μ_B . The parameter a_P is given in function of η_P with an excellent approximation by:

$$a_P = 3.172 \sqrt{\eta_P^2 - \eta_{P0}^2}, \quad (70)$$

where $\eta_{P0} = 0.13529$ (see Fig. 20). For $\eta_P < 0.135$, the normalized expression remains valid with an imaginary parameter $a_P = i a$. In this case the reduced Reynolds stress may

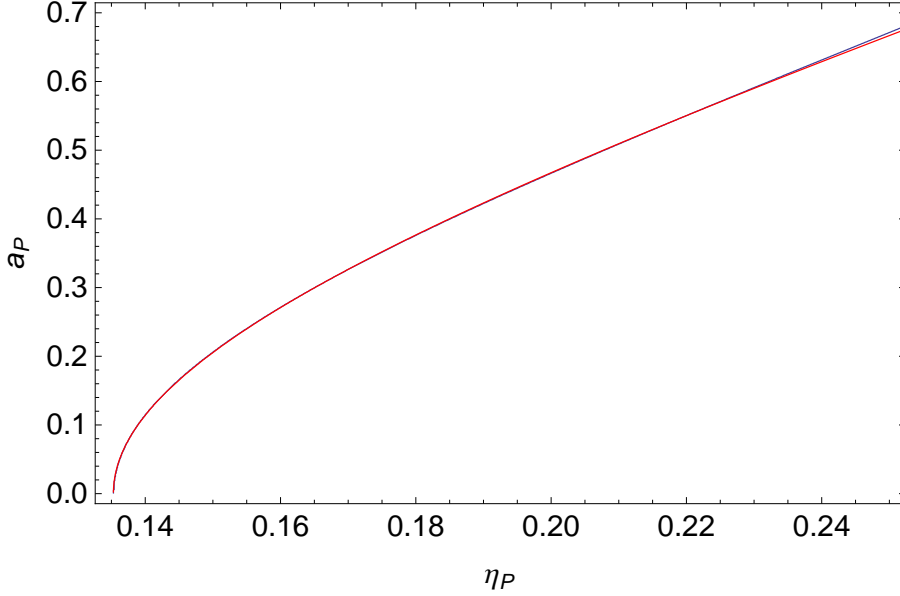


Figure 20: Variation of the parameter a_P in the reduced expression of the Reynolds stress $\sigma_{vr}^2 = \sqrt{\eta} \sin(a_P \ln \eta)$ in function of the position η_P of its maximum. The blue curve results from a numerical calculation while the red curve is the analytical approximation Eq. 70.

be also written in terms of real numbers as $\sigma_{vo}^2 = \sqrt{\eta/\eta_P} \times \sinh(a \ln \eta) / \sinh(a \ln \eta_P)$. Our solution for the Reynolds stress is plotted in Fig. 21 for various value of the peak position η_P .

Appendix B: various solutions of the equation $Q = \text{cst}$

We solve numerically the equation $Q(R, \mu_B, \eta_P, \alpha_B, \kappa; \eta) = 1$ by keeping only the values of the parameters for which the standard deviation σ_Q with respect to the flat profile $Q(\eta) = 1$ are small (typically $\sigma_Q < 0.002$) in the relevant range $\eta = 0.3 - 0.7$.

The expression of Q (Eq. 50) involves the Reynolds shear stress σ_{uv} , for which various theoretical solutions have been proposed [27]. The simplest is $\sigma_{uv} = 1 - \eta$ [4]. We have obtained a more elaborated solution which reads:

$$\sigma_{uv} = v_*^2 \left(1 - \eta \left(1 - \frac{\alpha_B}{\kappa^2} \ln \eta \right) \right), \quad (71)$$

while some experimental data yields slightly higher values (see Fig. 1 and references in its caption). We have considered these various possibilities in searching for a relation between the shear stress amplitude μ_B along the direction normal to the wall and the turbulent intensity ratio $R = \sigma_u / \sigma_v$.

We consider here the results of a run made with $\kappa = 0.4$ and the other parameters in the ranges $R = (1.2 - 1.6)$, $\mu_B = (0.8 - 1.6)$, $\alpha_B = (0.03 - 0.06)$ and $\eta_P = (0 - 0.4)$.

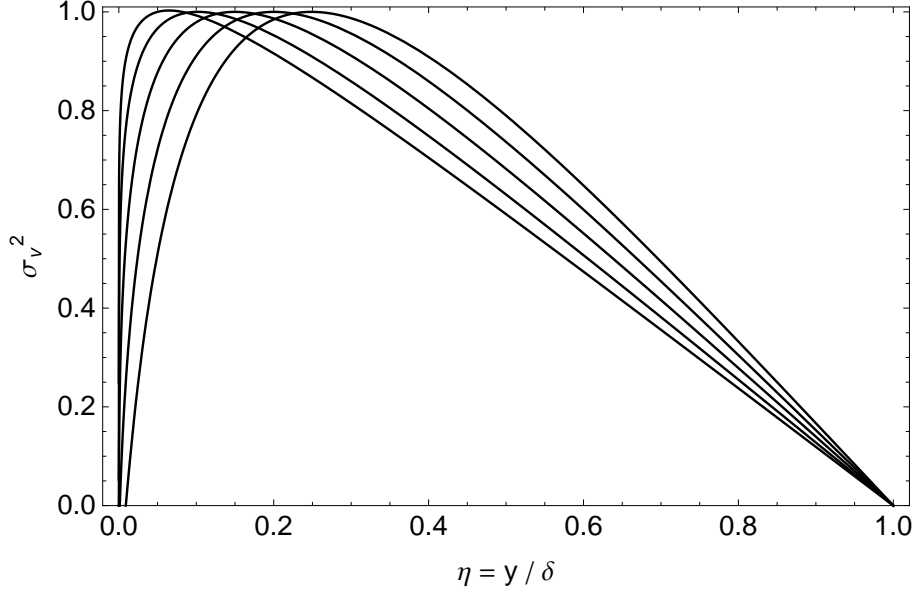


Figure 21: Solutions of the QHO v -Schrödinger equation for the Reynolds stress profiles σ_v^2 (Eq. 69). The function is normalized to $\sigma_v(\eta_P) = 1$, where η_P is the position of its maximum, and it is plotted for various values of this position, $\eta_P = 0.05, 0.10, 0.15, 0.20$ and 0.25 .

When using the approximate expression for $\sigma_{uv} = 1 - \eta$, a fit of the parameter subset such that $\sigma_\xi < 0.002$ yields, with a high statistical significance (Student $t > 45$ for the R coefficients):

$$\mu_B = 14.084 - 16.94 R + 5.57 R^2 - 5.34 \alpha_B + 37.11 \alpha_B^2 + 0.423 \eta_P. \quad (72)$$

Neglecting the dependence of μ_B on α_B and η_P which remains small, we obtain:

$$\mu_B(R) = R_0 - 2.18 (R - R_0) + 5.5 (R - R_0)^2, \quad (73)$$

where $R_0 = 1.33$ in that case.

When using the polynomial fit of [EJ] data for σ_{uv} (see Fig. 1), a fit of the parameter subset such that $\sigma_\xi < 0.002$ yields, with a high statistical significance (Student $t > 70$ for the R coefficients):

$$\mu_B = 12.182 - 13.00 R + 3.93 R^2 - 3.44 \alpha_B + 23.0 \alpha_B^2 - 2.79 \eta_P + 7.82 \eta_P^2. \quad (74)$$

Neglecting the small dependence of μ_B on α_B and η_P , we obtain:

$$\mu_B(R) = R_0 - 2.15 (R - R_0) + 4.0 (R - R_0)^2, \quad (75)$$

where $R_0 = 1.38$ in that case.

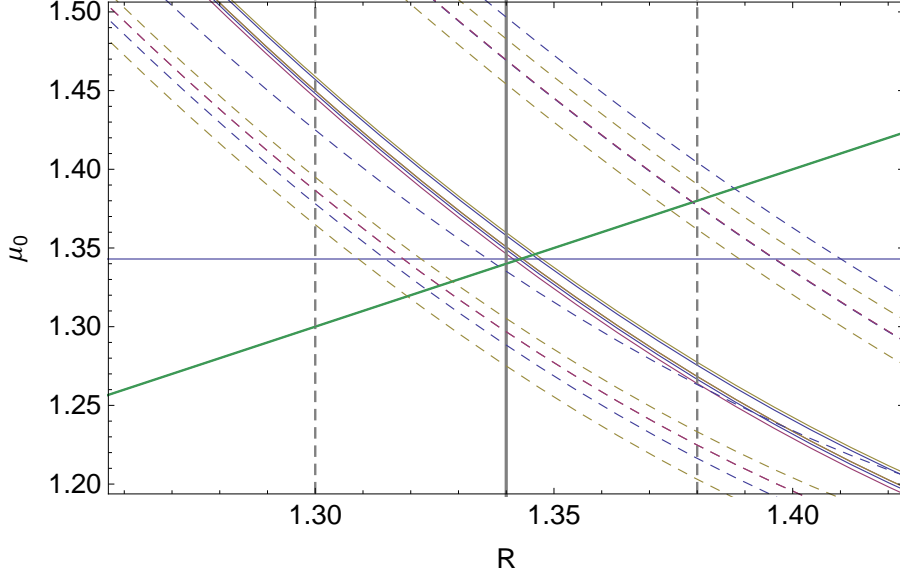


Figure 22: Relation $\mu_B(R)$ solving the equation $Q = \text{cst}$ (Eq. 50). The σ_v profile input in this equation is the theoretical solution of the k_v equation, while σ_{uv} is the solution of the RANS and continuity equations Eq. 52. The different continuous curves correspond to the range of possible values for α_B and η_P . The equality $\mu_B = R$ is reached for $R_0 = 1.344$. The dashed curves correspond to two others choices, the standard simple solution $\sigma_{uv} = 1 - \eta$ and a fit of [EJ] [28] data. It is compared to the range of predicted values for R from quantized QHOs, $R = 1.34 \pm 0.04$, yielding possible values for μ_B in the range (1.28 – 1.45).

Appendix C: analytic solution from power series

Power series of function Q Another way to obtain solutions for the equation $Q = 1$ consists of expanding Q in power series. Since we expect Q to be a constant independent from η , a linear expansion $Q = A(R, \mu_B) + B(R, \mu_B)(\eta - \eta_0)$ is sufficient and the searched solution is given by the slope cancellation $B(R, \mu_B) = 0$. Solving for this equation yields the solution $\mu_B = \mu_B(R)$, which depends also slightly on $(\alpha_B, \eta_P$ and $\kappa)$.

Since we already know that R lies in a restricted range $R \approx (1.3 - 1.4)$, we use linear expansions for R and for μ_B . The power series is performed in terms of $(R - R_0)$, $(\mu_B - \mu_{B0})$ and $(\eta - \eta_0)$ for various numerical values of the three remaining parameters, α_B , η_P , and κ . After expansion it takes the form:

$$Q = (a_0 + b_0 R + c_0 \mu_B + d_0 R \mu_B) + (a + b R + c \mu_B + d R \mu_B) \eta. \quad (76)$$

Thus the equation $Q = 1$ is translated into the slope cancellation equation $(a + b R + c \mu_B + d R \mu_B) = 0$, which leads to the searched solution:

$$\mu_B(R) = -\frac{a + b R}{c + d R}. \quad (77)$$

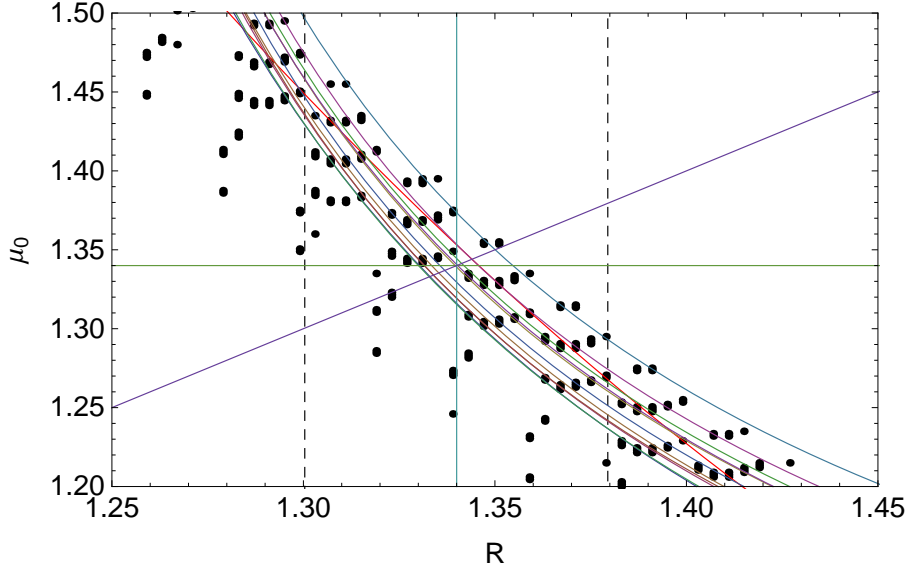


Figure 23: Comparison between the solutions of the equation $Q = \text{cst}$ obtained by fit with those obtained by power series. The solution by fit is given by the black points, which are values of R and μ_B such that the standard deviation of Q values around $Q = 1$ is $\sigma_Q < 0.002$. The dispersion between the points mainly comes from variation between the values of α_B and η_P . They have been slightly displaced in function of the values of these parameters in order to distinguish them (see Fig. 8 for a correction of their effect). The solutions by power series are found from the cancelation of the η coefficient in the linear expansion of $Q(\eta)$. The different curves correspond to $\alpha_B = (0.03, 0.045, 0.06)$, $\eta_P = (0.15, 0.175, 0.20)$ and $\kappa = (0.37, 0.40, 0.43)$.

We have taken $\eta_0 = 0.5$, $R_0 = 1.34$ and $\mu_{B0} = 1.34$, knowing that the final result is almost independent from this choice. These operations have been performed for numerical values of α_B , η_P and κ taken in their expected range (see caption of Fig. 23). The parameters (a, b, c, d) are found to weakly depend on these values. The result, plotted in Fig. 23, fully agrees with the previous fit method.

One finds a median solution given to lowest order by:

$$\mu_B = R_0 - 2.25 (R - R_0), \quad (78)$$

where $R_0 = 1.334$. Both the slope and the point R_0 for which $R = \mu_B$ essentially agrees with the result from the fit method.

The main variation comes from R while the other variables contribute only by $\approx \pm 0.02$. In order to be more specific on this point, we have performed a power series expansion for all parameters. We verify that the quadratic terms are small with respect to the linear ones. We set $n = \eta - \eta_0$, $r = R - R_0$, $m = \mu_B - \mu_{B0}$, $a = \alpha_B - \alpha_{B0}$, $p = \eta_P - \eta_{P0}$ and $k = \kappa - \kappa_0$. For example, performing an expansion of Q around $R_0 = \mu_{B0} = 1.344$, $\eta_0 = 0.5$, $\alpha_{B0} = 0.045$, $\eta_{P0} = 0.16$ and $\kappa_0 = 0.4$ we find:

$$Q = 1 - 0.026 n + 0.029 n^2 + 2.1 r - 0.59 m + 1.27 a + 3.6 p - 0.32 k, \quad (79)$$

manifesting a very flat variation with η as expected and a small dependence on the other parameters.

Full order two power series In order to get a more complete understanding of the behavior of the function $Q = Q(R, \mu_B, \alpha_B, \eta_P, \kappa; \eta)$ and of the way by which it can become constant, we have performed a full power series expansion of Q , linear in terms of η and up to order 2 in function of all the parameters. A full analytic form of the searched function $\mu_B = \mu_B(R, \alpha_B, \eta_P, \kappa)$ will then result from the cancellation of the η coefficient.

We have performed a power series expansion around the values $(R_0, \mu_{B0}, \alpha_{B0}, \eta_{P0}, \kappa_0) = (1.35, 1.35, 0.045, 0.16, 0.40)$, which are central with respect to the previously established possible range for these parameters. This allows us to now get an explicit form for the dependence of the relation $m(r)$ on the other parameters. After normalisation to 1 of the constant coefficient, we find:

$$\begin{aligned}
Q = & 1 - 0.5037 m + 2.167 r + 1.411 a + 4.378 p - 0.277 k \\
& + 1.127 m^2 + 3.59 r^2 - 12.92 a^2 - 0.60 p^2 + 1.21 k^2 \\
& + 2.513 mr + 2.27 ma - 2.97 mp + 1.03 mk + 9.65 ra \\
& + 7.78 rp + 1.38 rk + 13.7 ap - 3.91 ak - 1.64 pk \\
& + (0.0543 + 1.618 m + 3.764 r - 1.771 a + 1.070 p + 0.632 k \\
& - 0.0376 m^2 + 10.04 r^2 - 70.93 a^2 - 8.30 p^2 - 1.52 k^2 \\
& + 7.801 mr + 24.30 ma - 1.63 mp + 1.58 mk + 48.03 ra \\
& - 0.096 rp + 5.59 rk + 43.52 ap + 27.24 ak - 2.42 pk) n. \quad (80)
\end{aligned}$$

We express the constancy of Q by the cancellation of the coefficient of the n term. This equation is solved in terms of the function $m = m(r, a, p, k)$. We finally find a complete analytical expression for $m = \mu_B - 1.35$:

$$\begin{aligned}
m = & (-0.0336 + 1.596a - 0.694p - 0.357k - 13.04ak + 1.29k^2 - 14.90ap + 1.83kp) \\
& + (-2.161 - 5.079a + 1.297p + 0.421k + 62.82ak - 6.75k^2 + 48.91ap - 9.85kp) r \\
& + (4.317 - 39.45a - 2.18p - 6.36k - 177.3ak + 39.7k^2 - 249.5ap + 44.8kp) r^2. \quad (81)
\end{aligned}$$

The resulting function and its dispersion agree with its numerical determination as given in Fig. 23. In particular, its expression for $R = \mu_B = 1.35$, $\alpha_B = 0.045$, $\eta_P = 0.14$ and $\kappa = 0.4$ in the relevant range $R = (1.3 - 1.4)$ is very close to the fit of the numerical integration given by the red curve in Fig. 8. We show in Fig. 9 the function $m(r)$ for various values of the parameters. This analytical result supports our general conclusion according to which $\mu_B \approx R$. The value for which $\mu_B = R$ is found to be more precisely $R_0 = 1.34 \pm 0.01$.

Finally we have numerically checked the validity of this result by comparing the PDF of the standard deviation σ_Q of Q values relative to $Q = 1$ under the constraint given by Eq. 55, to the PDF obtained for all values without constraint. The result of this comparison is given in Fig. 24 and is very satisfactory. The PDF obtained while using the

analytic expression for μ_B shows a well defined peak at $\sigma_Q = 0.002$ then decreases with $\sigma_Q < 0.013$. This is in good agreement with the constraint $\sigma_Q < 0.002 - 0.005$ which we have used to numerically establish the $\mu_B(R, \alpha_B, \eta_P, \kappa)$ relation.

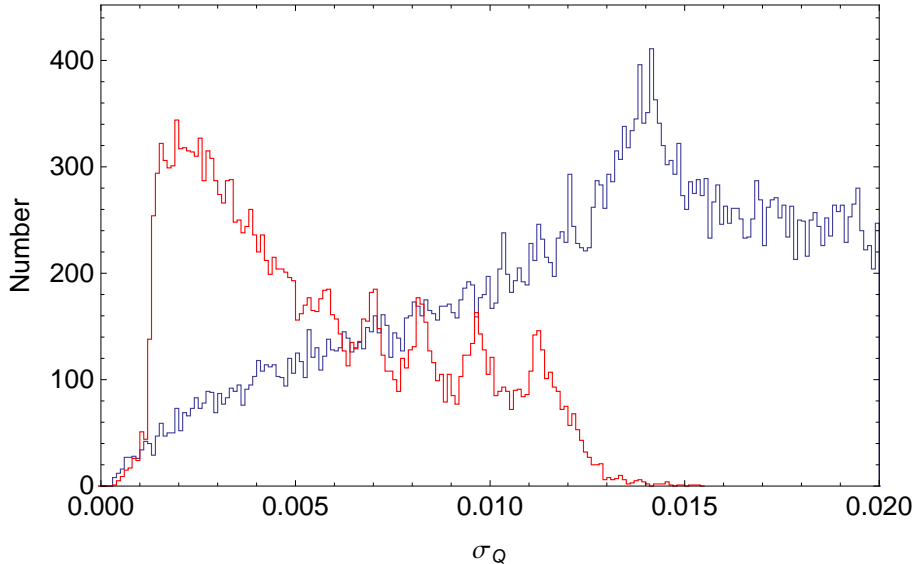


Figure 24: Comparison between the PDFs of standard deviations σ_Q under the constraint given by Eq. 55 (red histogram) to their PDF without constraint (blue histogram). The analytic μ_B expression has been obtained by cancelling the linear term $B = 0$ in the power series expansion $Q = A + Bn + \mathcal{O}[n^2]$. We have cut the no constraint PDF at $\sigma_Q = 0.02$, but it actually continues without decreasing up to large values ~ 1 .

Remark that this solution, obtained from the cancellation of the linear term of $Q(n)$, though satisfactory since agreeing with the numerical results, cannot be considered as yet optimal. Indeed, the profile with smallest dispersion around $Q = 1$, may have a slope which is small but nevertheless non-zero at $n = 0$. Actually, as can be seen in Fig. 7, the profiles for which the standard deviation σ_Q with respect to $Q = \text{cst}$ are the smallest have a W-like shape which are characteristic of polynomials of order at least η^4 , with a negative parabolic contribution $-\eta^2$. We have compared these profiles with their power series expression and found that a complete agreement can be obtained in every case only at order η^6 or η^8 . A more detailed analysis of this behavior will be presented in a future work. In particular, we expect to recover in an analytic way the various properties which have been obtained by numerical methods (PDFs of parameters and relations between them).

References

- [1] T. von Karman, “Mechanische Ähnlichkeit und Turbulenz”, In Proc. Third Int. Congr. Applied Mechanics, Stockholm, pp. 85-105 (1930).

- [2] L. Prandtl, “Zur Turbulenten Strömung in Rohren und längs Platten”, *Ergeb. Aerod. Versuch Göttingen*, IV Lieferung, 4 (1932).
- [3] A.N. Kolmogorov, “The local structure of turbulence in incompressible viscous fluid for very large Reynolds numbers”, *C. R. Acad. Sci. URSS* **30**, 301 (1941).
- [4] H. Tennekes & J.L. Lumley, *A first course in turbulence*, MIT Press, Cambridge, Massachusetts (1972).
- [5] S.B. Pope, *Turbulent Flows*, Cambridge University Press (2000).
- [6] H. M. Nagib and K. A. Chauhan, “Variations of von Karman coefficient in canonical flows”, *Physics of Fluids* 20, 101518 (2008).
- [7] S. Bailey, M. Vallikivi, M. Hultmark, & A. Smits, “Estimating the value of von Karman’s constant in turbulent pipe flow”, *Journal of Fluid Mechanics*, 749, 79 - 98 (2014).
- [8] W. K. George, “Is there a universal log law for turbulent wall-bounded flows?”, *Philosophical Transactions of the Royal Society A: Mathematical, Physical and Engineering Sciences*, 365(1852), 789-806 (2007).
- [9] G. Smart, “A base for the log law and von Karman’s constant problem”, *Journal of Hydraulic Research* 60 : 6, 935 - 943 (2022).
- [10] L. Nottale and T. Lehner, “The Turbulent Jet in the Scale-Relativity Framework”, hal-04272392 (2023), submitted for publication
- [11] H.S. Shafi and R.A. Antonia, “Anisotropy of the Reynolds stresses in a turbulent boundary layer on a rough wall”, *Experiments in Fluids*, 18(3), 213-215 (1995).
- [12] C.E. Brennen, “Internet book on fluid dynamics”, *Dankat Publishing* (2016).
- [13] P. R. Spalart, “Direct simulation of a turbulent boundary layer up to $Re = 1410$,” *J. Fluid Mech.* 187, 61 (1988).
- [14] M. Inoue, “Large-eddy simulation of the flat-plate turbulent boundary layer at high Reynolds numbers”, PhD thesis, California Institute of Technology (2012)
- [15] J. Kim, P. Moin, and R. Moser. “Turbulence statistics in fully developed channel flow at low Reynolds number”, *J. Fluid Mech.* 177, 133-166 (1987).
- [16] L. de Montera, “A theory of turbulence based on scale relativity”, arXiv:1303.3266 (2013).
- [17] L. Nottale, “Relativity of Scales, Fractal Space-Time and Quantum Potentials”, in *Space-Time Geometry and Quantum Events*, edited by I. Licata (Nova Science, 2014), Chap. 5.

- [18] L. Nottale and T. Lehner, “Turbulence and scale relativity”, *Phys. Fluids* 31, 105109 (2019).
- [19] L. Landau and E. Lifchitz, *Fluid Mechanics* (Pergamon Press, Oxford, 1980).
- [20] U. Frisch, *Turbulence: The Legacy of A.N. Kolmogorov* (Cambridge University Press, 1995).
- [21] L. de Montera, T. Lehner, W. Mouhali and L. Nottale, “Describing geophysical turbulence with a Schrödinger-Coriolis equation in velocity-space”, *Physics of Fluids* 36, 015136 (2024)
- [22] L. Nottale, *Fractal Space-Time and Microphysics: Towards a Theory of Scale Relativity* (World Scientific, Singapore,1993).
- [23] L. Nottale *Scale Relativity and Fractal Space-Time: a New Approach to Unifying Relativity and Quantum Mechanics* (Imperial College Press, London, 2011).
- [24] L. Nottale, “Generalized quantum potentials”, *J. Phys. A: Math. Theor.* **42**, 275306 (2009).
- [25] H. Schlichting (1979), “Boundary-Layer Theory”, 7 th ed., McGraw Hill, New York, U.S.A. (1979).
- [26] D. E. Coles, “The law of the wake in the turbulent boundary layer,” *J. Fluid Mech.* 1, 191 (1956).
- [27] R. J.Volino, and M. P. Schultz, “Determination of wall shear stress from mean velocity and Reynolds shear stress profiles”, *Phys. Rev. Fluids* 3, 034606 (2018).
- [28] L.P. Erm and P.N. Joubert, “Low-Reynolds-number turbulent boundary layers”, *J. Fluid Mech.* 230, 1-44 (1991).
- [29] B. Brzek, R. Bayoan Cal, G. Johansson & L. Castillo, “Inner and outer scalings in rough surface zero pressure gradient turbulent boundary layers”, *Phys. Fluids* 19, 065101 (2007).
- [30] L. Landau and E. Lifchitz, *Statistical Physics* (Pergamon Press, Oxford, 1987).
- [31] A. A. Townsend, “The properties of equilibrium boundary layers”, *J. Fluid Mech.* 1, 561-573 (1956).
- [32] H. P. Bakewell Jr & J. L. Lumley, “Viscous sublayer and adjacent wall region in turbulent pipe flow”, *The Physics of Fluids*, 10, 1880-1889 (1967).
- [33] M. Uhlman, “Turbulences flows and their modeling”, www.ifh.uni-karlsruhe.de/people/uhlmann (2008)

- [34] J. Jimenez, S. Hoyas, M.P. Simens, & Y. Mizuno, “Turbulent boundary layers and channels at moderate Reynolds numbers”, *J. Fluid Mech.* 657, 335 - 360 (2010).
- [35] J.A. Businger, et al., “Flux profile relationships in the atmospheric surface layer”, *J. Atmos.Sci.*, 28, 181-189 (1971).
- [36] P.A. Sheppard, “The aerodynamic drag of the Earth’s surface and the value of Karman’s constant in the lower atmosphere”, *Proc. Roy. Soc. London Ser. A*, 188, 208-222 (1947).
- [37] M. Lee, & R. Moser, “Direct numerical simulation of turbulent channel flow”, *J. Fluid Mech.* 774, 395-415 (2015).
- [38] Z. S. She, X. Chen & F. Hussain, “Quantifying wall turbulence via a symmetry approach: a Lie group theory”, *Journal of Fluid Mechanics*, 827, 322-356 (2017).
- [39] N. R. Panchapakesan & J.L. Lumley, “Turbulence measurements in axisymmetric jets of air and helium. Part 1. Air jet”, *J. Fluid Mech.* **246**, 197 (1993).
- [40] H.J. Hussein, S.P. Capp & W.K. George, “Velocity measurements in a high-Reynolds-number, momentum-conserving, axisymmetric, turbulent jet”, *J. Fluid Mech.*, **258**, 31 (1994).
- [41] J.A. Sillero, J. Jimenez & R.D. Moser, “One-point statistics for turbulent wall-bounded flows at Reynolds numbers up to 2000”, *Phys. Fluids* 25, 105102 (2013).
- [42] A.G. Gungor, Y. Maciel, M. P. Simens & J. Soria, “Analysis of a Turbulent Boundary Layer Subjected to a Strong Adverse Pressure Gradient”, *J. Phys.: Conf. Ser.* 506 012007 (2014).